



## Characterization and origin of granites from the Luoyang Fe deposit, southwestern Fujian Province, South China



Zhen-Jie Zhang<sup>a,\*</sup>, Qiu-Ming Cheng<sup>b</sup>, Jie Yang<sup>b</sup>, Xin-Lu Hu<sup>c</sup>

<sup>a</sup> School of Earth Sciences and Resources, China University of Geosciences, Beijing 100083, China

<sup>b</sup> State Key Laboratory of Geological Processes and Mineral Resources, China University of Geosciences, Beijing 100083, China

<sup>c</sup> Faculty of Earth Resources, China University of Geosciences (Wuhan), Wuhan 430074, China

### ARTICLE INFO

**Keywords:**

Luoyang Fe deposit  
Luoyang granite  
Makeng-type deposit  
Origin of granite

### ABSTRACT

The Luoyang Fe deposit, located in southwestern Fujian Province (South China), is one of the Makeng-type skarn Fe deposits (i.e., skarn Fe deposits related to granite) related to the late Yanshanian (i.e., Early Cretaceous) granite. To better understand different mineral assemblages in different deposits, geochemistry and isotopic systematics of the granite magma source of the Luoyang Fe deposit were compared with those of other Makeng-type skarn Fe deposits in southwestern Fujian Province. Laser ablation inductively coupled plasma mass spectrometry (LA-ICP-MS) zircon U-Pb dating of the nearby exposed Luoyang fine-grained granite and porphyritic granite yielded weighted mean  $^{206}\text{Pb}/^{238}\text{U}$  ages of  $139.6 \pm 1.4$  Ma and  $137.2 \pm 2.3$  Ma, respectively. The Luoyang granite exhibits geochemical characteristics of highly fractionated I-type to A-type, consistent with the Pantian (PT) and Zhongjia (ZJ) granites in the Pantian and Zhongjia Fe deposits; whereas, the Dapai (DP) and Dayang-Juzhou (DJ) granites in the Dapai and Makeng Fe deposits show unfractionated I- and relatively typical A-type characteristics, respectively. It can be inferred from whole rock Sr-Nd-Pb and zircon Hf isotopes that the source magma of the Luoyang granite is coincident with other skarn Fe mineralization related granites of the Makeng-type deposits in southwestern Fujian Province. The magma was derived from partial melting of the Proterozoic metasedimentary Cathaysia basement rocks. Underplating of mafic magma in the depleted mantle and/or lower tholeiitic crust was also involved, which provided the heat source for partial melting. The change in tectonic environment and the different mafic sources involved caused significant differences in the Fe metallocgenesis in southwestern Fujian Province.

### 1. Introduction

The Luoyang deposit (> 367 Mt ore reserves @ > 45% total Fe) is one of the most important Fe deposits in Fujian Province. The Fe mineralization and skarn alteration are distributed between the Early Carboniferous Lindi Formation sandstones and the Late Carboniferous Chuanshan Formation limestones, and between the carbonates and granite. The granite in the Luoyang deposit intrudes along with the NE-trending regional Zhenghe-Dapu Fault. Wang et al. (2015b) and Zuo (2016) explored the spatial distribution characteristics of the Makeng-type skarn Fe deposits in Fujian Province, and suggested that these Fe deposits have a nonlinear spatial relationship with the Yanshanian granitic intrusions, Carboniferous-Permian clastic and carbonic rocks, and NNE-NE-trending faults. In addition, molybdenite, syngenetic with magnetite in the Luoyang Fe deposit, has yielded Re-Os ages of 133 ( $\pm 1.9$ )-(134 ( $\pm 4.2$ ) Ma (Zhang et al., 2012d). This is similar to an age of 131 Ma for the granite of the Luoyang deposit, obtained by laser

ablation inductively coupled plasma mass spectrometry (LA-ICP-MS) zircon U-Pb dating (Zhang et al., 2012d). Therefore, the Luoyang deposit is spatially and temporally related to the late Yanshanian (i.e., Early Cretaceous) granite, which is synchronous with the other Makeng-type skarn Fe deposits in southwestern Fujian Province; for example, Makeng (Zhang and Zuo, 2014; Zhang et al., 2015a, 2015b), Pantian (Lai et al., 2014), Dapai (Yuan et al., 2013; Zhao et al., 2016), and Zhongjia (Niu et al., unpublished work).

However, the Makeng Fe deposit related to the Dayang-Juzhou (DJ) granite is associated with molybdenum, whereas the Zhongjia Fe deposit related to the Zhongjia (ZJ) granite is associated with cassiterite, and the Dapai Fe deposit related to the Dapai (DP) granite is associated with galena and sphalerite (Yang et al., 2008; Zhang et al., 2012c, 2015b; Yuan, 2014; Zhao et al., 2016). It is unclear what lead to different mineral assemblages in different deposits. In addition, the geochemical and isotopic characteristics of the mineralized granite in Luoyang deposit are still poorly known. In this study, we investigated

\* Corresponding author.

E-mail addresses: [zjzhang@cug.edu.cn](mailto:zjzhang@cug.edu.cn), [zzj1117@126.com](mailto:zzj1117@126.com) (Z.-J. Zhang).

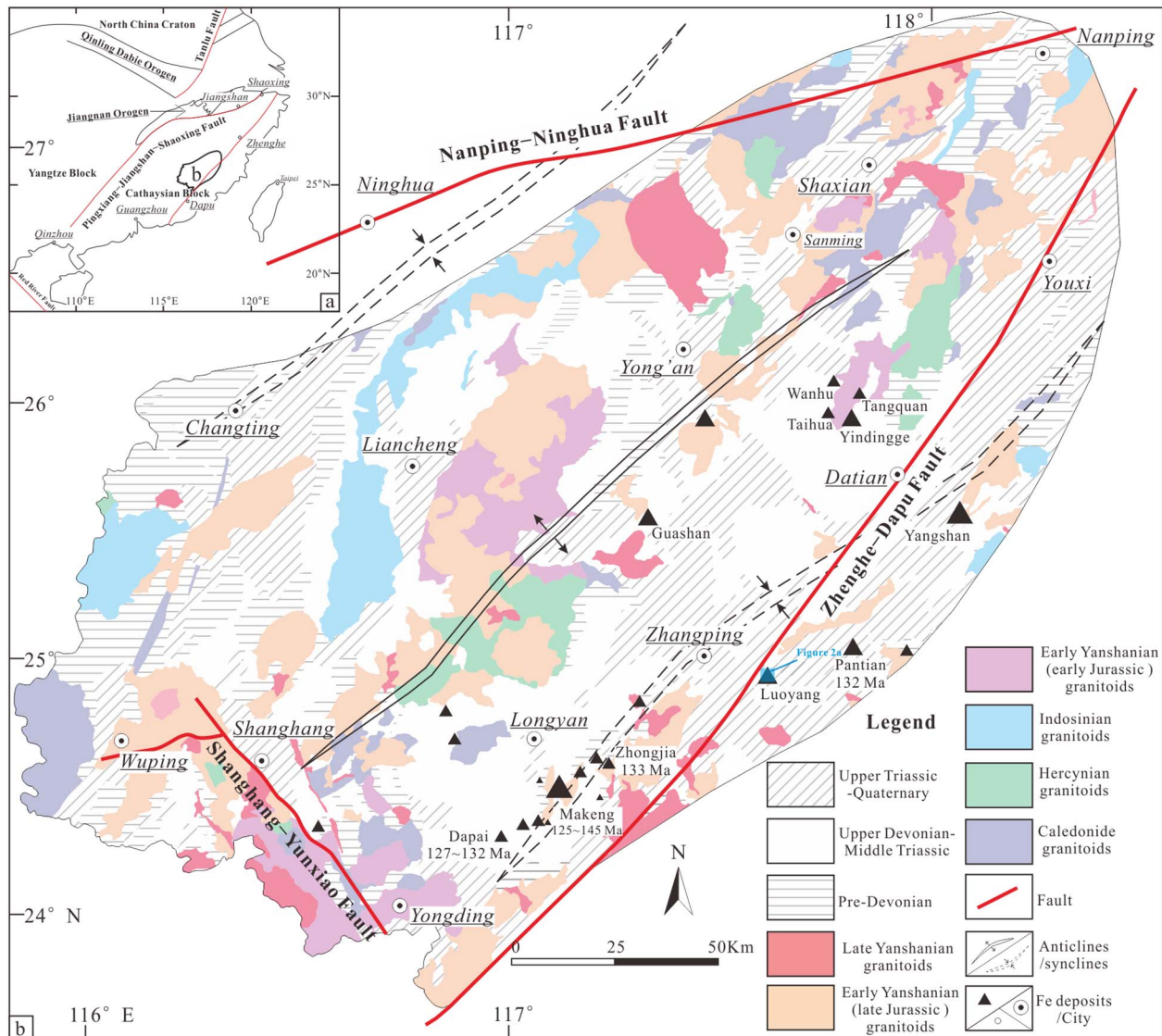


**Fig. 1.** Geologic setting of South China (a, modified after Li et al., 2003b; Zuo et al., 2015) and geological map of southwestern Fujian Province (b, modified after Lin, 2011; Zuo et al., 2015). Age data from Makeng Fe deposit after Zhang et al. (2015b); age data from Dapai Fe deposit after Yuan et al. (2013); age data from Pantian Fe deposit after Lai et al. (2014); age data from Zhongjia Fe deposit after Yang et al. (2008).

the geochemistry, zircon U-Pb isotopic dating and Lu-Hf isotope analyses, and Rb-Sr, Sm-Nd, and Pb isotope analyses of the granites in the Luoyang deposit area. These data are used to discuss the geodynamic setting of the mineralization of the Luoyang deposit in comparison with the other Makeng-type skarn Fe deposits of southwestern Fujian Province.

## 2. Geological background

### 2.1. Geologic setting

The Luoyang Fe deposit is located near Zhangping City, Fujian Province, South China. The geology and tectonic evolution of South China, consisting of the Yangtze and Cathaysian blocks (Fig. 1a), have been extensively described (e.g., Xu et al., 1987; Shu and Zhou, 1988; Li, 1993; Guo et al., 1996; Chen and Xiao, 1998; Li et al., 2002, 2003a, 2003b; Mao et al., 2004; Shu, 2006; Shu et al., 2008, 2009a, 2009b, 2011). Mesozoic tectonic and magmatic events are important to the mineralization in southwestern Fujian Province. Most scholars (Shu and Zhou, 2002; Mao et al., 2004, 2007, 2008) have divided the Mesozoic tectonic and magmatic events in South China into two stages: the

Indosinian (Late Permian–Middle Triassic) and Yanshanian (Jurassic–Cretaceous). In the early Indosinian, South China evolved from a marine to a terrestrial environment, followed by intracontinental collisional orogeny. Approximately E–W trending folds are regarded as a remote response to early Indosinian collisional orogenic and subduction–accretion events on the north and south margins of South China (Mao et al., 2001; Xie et al., 2001). Mao et al. (2004, 2007, 2008) proposed tectonic domain rotation from the E–W-trending Tethyan to NE-trending Pacific in the Middle–Late Jurassic. Several tectonic models have been proposed to explain the occurrence of such large-scale anorogenic magmatism during the Jurassic and Cretaceous in South China; for example, changes in the subduction angle (Zhou and Li, 2000; Shu and Zhou, 2002; Zhang et al., 2009), subduction speed (Wang et al., 2005), and subduction direction (Mao et al., 2004, 2007).

### 2.2. Geology of southwestern Fujian Province

The Luoyang Fe deposit is located in the southeast synclinal basin of the early Hercynian Yong'an–Meixian fold belt. In this district, several similar Fe deposits have been discovered, (e.g., the Makeng, Pantian, Zhongjia, Zhangkeng, Qinshan, Yangshan, and Dapai Fe deposits), all of

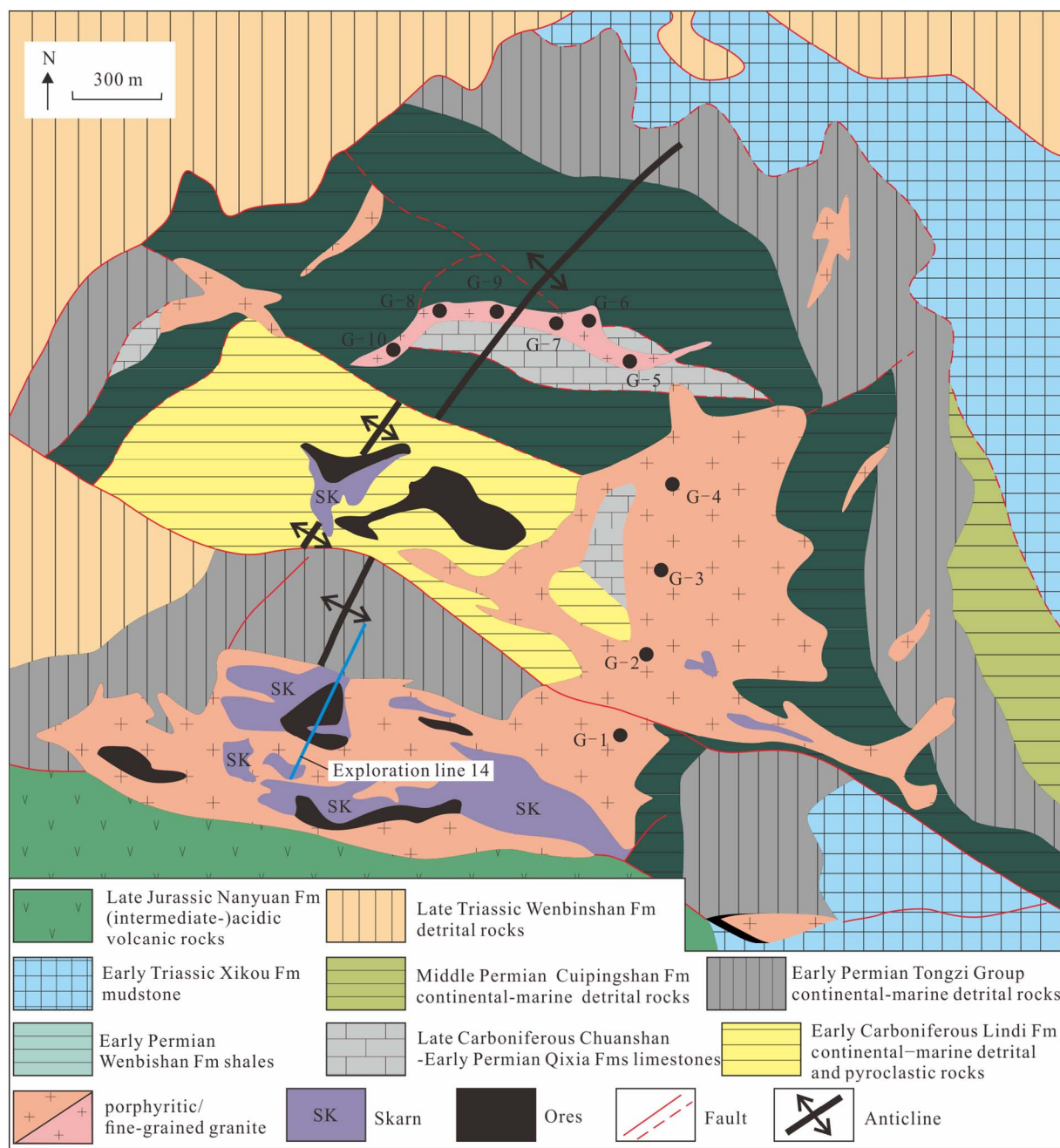


Fig. 2. Geological map of Luoyang Fe deposit (modified after Huang, 2011; black circles are sample locations).

which are located on the sides of the NE-trending Zhenghe-Dapu Fault (Fig. 1b).

Late Paleozoic marine sedimentary rocks, discontinuously distributed along the regionally NE-trending Zhenghe-Dapu Fault, are the dominant lithologies in southwestern Fujian Province (Han and Ge, 1983). The primary ore-hosting strata are the Middle-Lower Carboniferous clastic and carbonate rock formations.

In addition, voluminous granitoids are emplaced in the region. The majority of these were intruded during the Indosinian and Yanshanian stages, and a few were intruded during the Caledonian and Hercynian orogenies. Granitoids intruded almost all the Fe deposit districts in southwestern Fujian Province.

The most conspicuous structures in southwestern Fujian Province are the Zhenghe-Dapu, Nanping-Ninghua, and Shanghang-Yunxiao faults (Fig. 2). The first two faults define the southeastern and northern boundaries of the southwestern Fujian Province, extending along strike

orientations of approximately 60° and 15°, respectively, for over 300 km (Fig. 2). The Zhenghe-Dapu Fault, which experienced pre-Caledonian-Caledonian and Indosinian ductile shear deformation, late Indosinian-early Yanshanian thrust napping, and Yanshanian-Himalayan extension-detachment, is the most important structure in southwestern Fujian Province (Shui et al., 1993). The early Hercynian Yong'an-Meixian fold belt is another prominent structural feature. It was formed during the closure of the Paleotethys Ocean in the Late Devonian-Early Triassic (Shu et al., 2004). It overlies the Caledonian basement, and strikes along a length of over 200–300 km with a NE-trending axis. All the discovered Fe deposits in southwestern Fujian Province are distributed in the southeast synclinal basin (Fig. 2). Secondary NW- and NE-trending faults and folds are also widespread within this district.

The major ore bodies in Makeng deposit are hosted between sandstone and carbonate formations. The DJ granitic intrusion, emplaced on

the two sides and the bottom of Makeng deposit district, is composed of porphyritic biotite granite and fine-grained syenogranite. Several different zircon U-Pb ages, have been obtained (e.g.,  $127.5 \pm 0.4$  Ma,  $129.6 \pm 0.8$  Ma,  $132.6 \pm 1.3$  Ma,  $133.8 \pm 1.0$  Ma,  $136 \pm 1.7$  Ma,  $140.2 \pm 1.1$  Ma,  $140.1 \pm 1.0$  Ma and  $144.8 \pm 0.9$  Ma) using the Sensitive High Resolution Ion Microprobe (SHRIMP) or LA-ICP-MS methods (Mao et al., 2006; Zhang et al., 2012c; Zhang et al., 2015b). The ore bodies in Pantian and Zhongjia deposits also mainly occur in silico-calcium lithologic boundaries in the outer contact zone of the granite. The LA-ICP-MS zircon U-Pb dating of the PT and ZJ porphyritic biotite granites indicate intrusive ages of  $131.7 \pm 0.5$  Ma (Lai et al., 2014) and  $132.5 \pm 2.5$  Ma (Niu, unpublished data), respectively. The ore bodies of Dapai deposit, by contrast, are mostly distributed in carbonate formations. The LA-ICP-MS and SHRIMP zircon U-Pb age of  $132.4 \pm 0.8$  Ma and  $127.0 \pm 1.8$  Ma have been reported for the monzonitic granite and granodiorite intruded in the deposit district, respectively (Yuan et al., 2013; Zhao et al., 2016).

### 2.3. Geology of the Luoyang Fe deposit

The Carboniferous and Permian sequences are the dominant rock units in the Luoyang Fe deposit district (Figs. 2 and 3). Early Carboniferous Lindi formation (Fm) consists of a series of continental-marine detrital and few pyroclastic rocks; whereas, the Late Carboniferous Chuanshan and Early Permian Qixia Fms are mainly composed of various offshore shallow sea sedimentary and impure limestones. The Early Permian Wenbian Fm and Tongzi Group, and the Middle Permian Cuipingshan Fm contain sandstone, conglomerate, argillite, siltstone, and shale (Huang, 2011; Zhang et al., 2012d).

The Yanshanian Luoyang granitic stock, outcropping  $< 1$  km $^2$  (Figs. 2 and 3), is composed of pink porphyritic granite and pink fine-grained granite. The outcropping area of fine-grained granite is smaller

than that of the porphyritic granite; however, it is actually a stock in the bottom of the Luoyang deposit. The porphyritic granite, which is more vein-shaped in comparison, cuts through the fine-grained granitic stock.

The sedimentary rocks form an anticlinorium, on which the smaller NNE-SSW-oriented Luoyang subsidiary anticline is locally observed. The fold is destroyed and transformed by the Yanshanian Luoyang granitic intrusion; therefore, the orebodies and skarns are primarily located along the decollement of the Luoyang subsidiary anticline axis (Fig. 2). NW-oriented and several NE-NNE-oriented faults are present in the deposit district (Fig. 2). These faults, commonly formed before Fe mineralization, are accommodation structures and are filled by skarns and ore rocks.

The Fe mineralization and skarn alteration are hosted between the Lindi Fm sandstones and Chuanshan Fm carbonates, and between the Chuanshan-Qixia Fms carbonates and the granite (Fig. 3). Rocks in the contact zone between the Lindi Fm sandstones and Chuanshan-Qixia Fms limestones, and between the Chuanshan-Qixia Fms limestones and granite are commonly transformed into marble and skarn assemblages (Fig. 4a). Endoskarn, where some fine Fe- and Mo-mineralization and skarn alteration veins cut through the granite, can be found on the granite side of the contact zone between limestones and granite (Fig. 4b). Exoskarn, containing garnet- and pyroxene-dominant prograde calc-silicate assemblages with massive magnetite (Fig. 4c-f), is much more abundant than the endoskarn.

## 3. Samples and analytical methods

### 3.1. Granite samples

Four porphyritic granite and six fine-grained granite samples, representative and fresh, were collected from the Luoyang granitic pluton for (Fig. 2). The porphyritic granite, with phenocrysts (orthoclase and

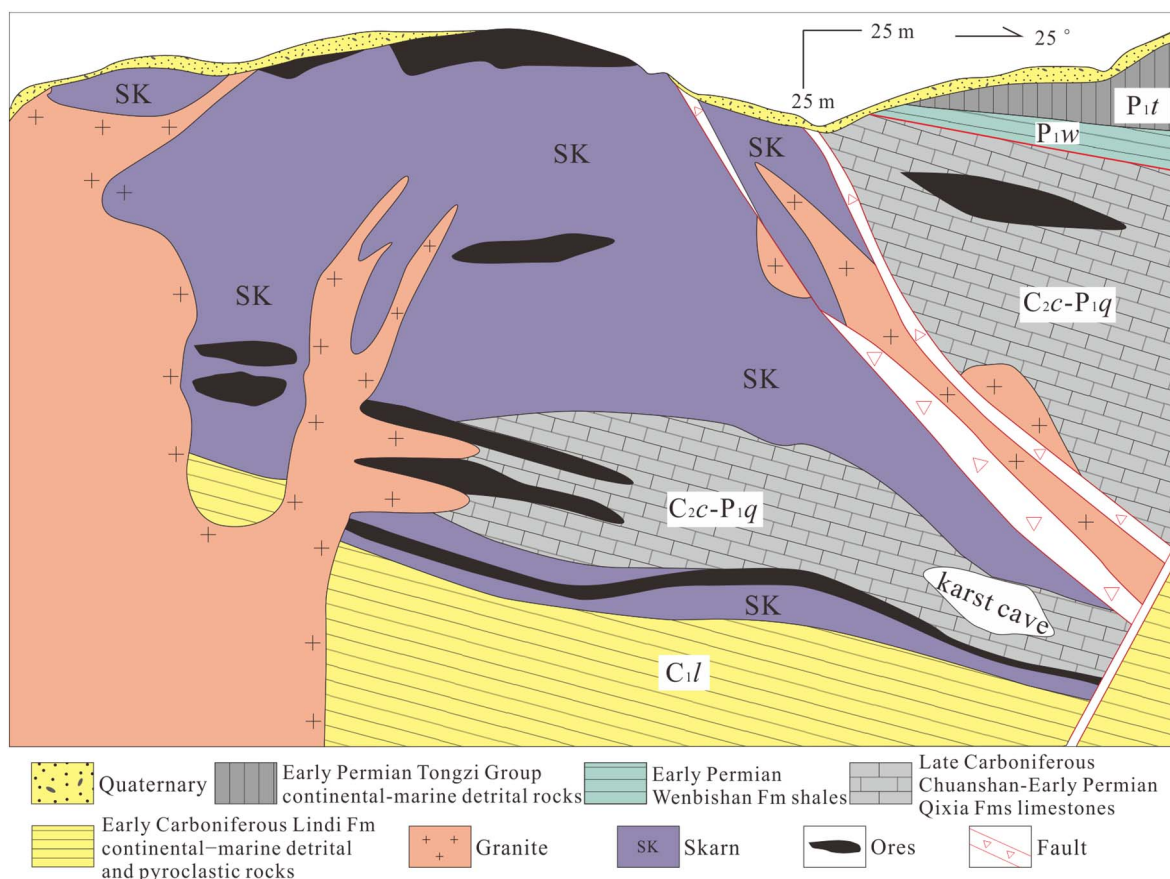
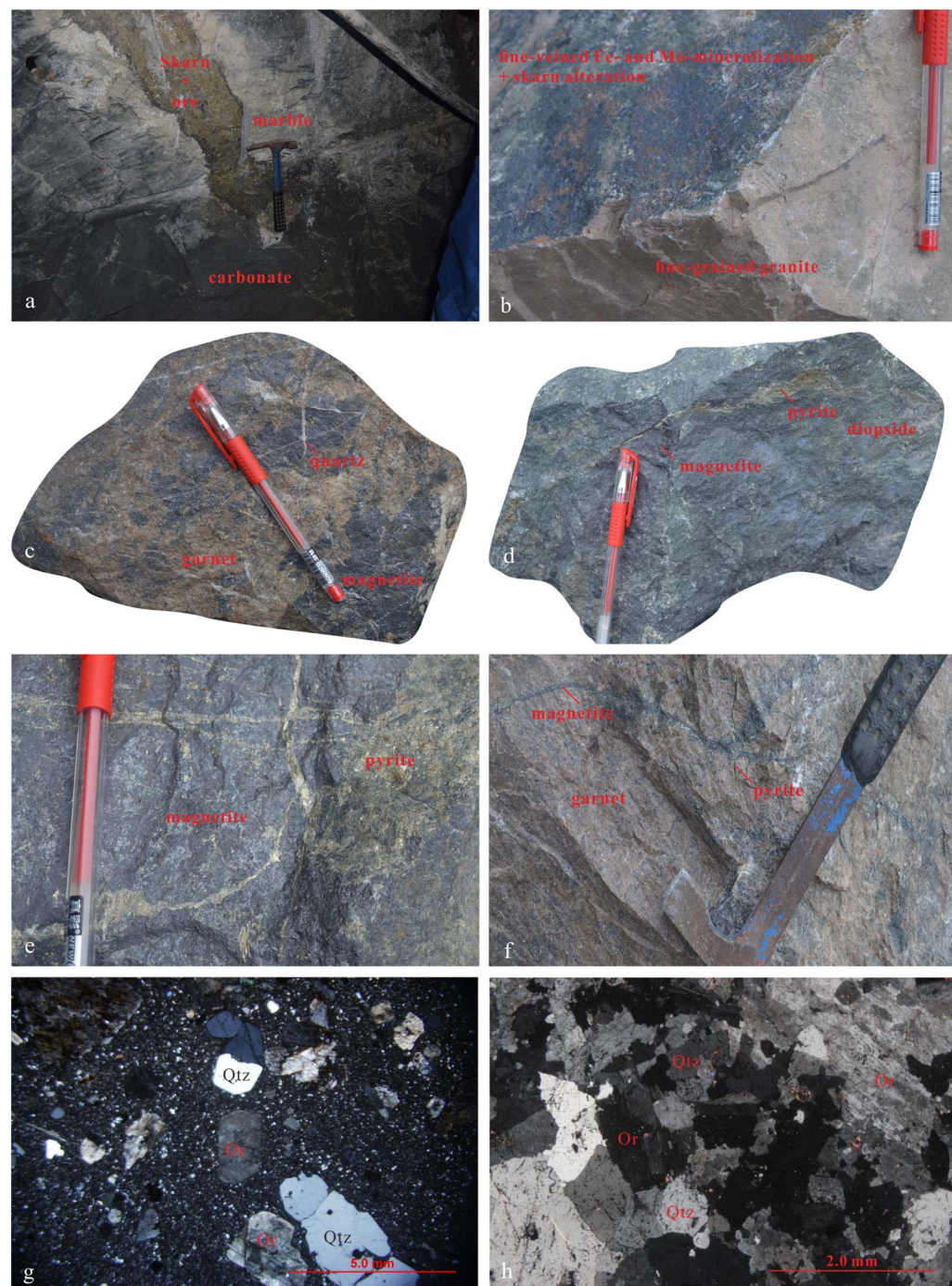


Fig. 3. Profile of the Exploration line 14 (modified after Huang, 2011).



**Fig. 4.** Photographs showing the skarn alteration, Fe mineralization and granite (microscope) in the Luoyang deposit. (a) the skarn with some magnetite vein in the Chuanshan Formation carbonate and the carbonate near skarn turned to marble; (b) the fine-veined skarn with some Fe + Mo-mineralization in the endoskarn; (c) the garnet-dominant ore and the early garnet and magnetite crosscut by the later quartz vein; (d) the diopside-dominant ore and the early diopside and magnetite crosscut by the later pyrite vein; (e) the massive ore with the early magnetite crosscut by the later pyrite vein; (f) the early garnet crosscut by the later magnetite vein which crosscut by the more later pyrite vein; (g), (h) the microscope photographs for porphyritic granite and fine-grained granite, Qtz-quartz, Or-orthoclase.

quartz) of approximately 0.5 cm and matrix (orthoclase, quartz, albite and amphibole) of < 0.1 cm, is typically composed of orthoclase (~55 vol%), quartz (~30 vol%), albite (~10 vol%), and amphibole (~5 vol%); whereas the fine-grained granite (~0.01–0.1 cm) consists of orthoclase (~60 vol%), quartz (~25 vol%), albite (~10 vol%), and amphibole (< 5 vol%; Fig. 4g–h).

### 3.2. Granite major and trace element analysis

Four porphyritic granite and six fine-grained granite samples were used for major and trace element analysis. Rock powders (< 200 mesh) were obtained with an agate mill.

Major element concentrations were obtained by the Axios Max X-ray Fluorescence Spectrometer with analytical uncertainties of 5%.

Trace elements, including rare earth elements (REEs), were determined using an Agilent 7500a ICP-MS with analytical precision of better than 5% for most elements. The detailed analytical procedures employed were the same as those described by Liu et al. (2008). Granite major and trace element analyses were performed at the State Key Laboratory of Geological Processes and Mineral Resources (GPMR), China University of Geosciences (Wuhan) (CUG).

### 3.3. Zircon U-Pb dating and Hf isotope analysis

One porphyritic granite sample (G-3) and one fine-grained granite sample (G-8) were collected from the Luoyang granitic pluton for age analysis. Pure zircon separates were hand-picked from the 60–80 mesh size chips crushed by a motor-driven agate mortar. (Cross-) polarized

**Table 1**

Chemical compositions for the Luoyang granite.

Sample no.	G-1	G-2	G-3	G-4	G-5	G-6	G-7	G-8	G-9	G-10
Type	Porphyritic granite					Fine-grained granite				
<i>Major oxides (%)</i>										
SiO <sub>2</sub>	76.04	74.20	75.31	75.57	75.21	76.16	76.86	75.21	72.45	75.84
Al <sub>2</sub> O <sub>3</sub>	12.61	13.48	12.94	12.81	12.47	12.42	12.11	12.53	13.07	12.24
Fe <sub>2</sub> O <sub>3t</sub>	1.08	1.58	1.28	1.30	1.22	0.88	0.96	0.96	1.17	1.28
FeO <sub>t</sub>	0.97	1.42	1.15	1.17	1.10	0.79	0.86	0.86	1.05	1.15
MgO	0.22	0.25	0.25	0.20	0.10	0.04	0.03	0.08	0.38	0.09
CaO	0.24	0.18	0.28	0.26	1.08	0.72	0.45	0.83	1.44	0.98
Na <sub>2</sub> O	3.23	3.19	3.38	3.36	3.15	3.75	3.47	2.74	2.79	3.21
K <sub>2</sub> O	4.62	4.70	4.51	4.53	4.87	4.42	4.91	5.98	6.41	4.47
TiO <sub>2</sub>	0.19	0.25	0.21	0.20	0.08	0.08	0.09	0.08	0.28	0.09
P <sub>2</sub> O <sub>5</sub>	0.04	0.03	0.05	0.07	0.02	0.02	0.02	0.02	0.06	0.02
MnO	0.06	0.07	0.07	0.07	0.05	0.02	0.01	0.04	0.03	0.05
H <sub>2</sub> O <sup>−</sup>	0.30	0.26	0.26	0.24	0.12	0.02	0.02	0.08	0.12	0.04
LOI	1.48	1.80	1.66	1.46	1.36	0.90	0.94	1.24	1.94	1.38
Total	98.33	97.93	98.28	98.36	98.24	98.52	98.91	98.47	98.08	98.27
Na <sub>2</sub> O + K <sub>2</sub> O	7.85	7.89	7.89	7.89	8.02	8.17	8.38	8.72	9.20	7.68
K <sub>2</sub> O/Na <sub>2</sub> O	1.43	1.47	1.33	1.35	1.55	1.18	1.41	2.18	2.30	1.39
Molar A/CNK	1.17	1.26	1.18	1.17	1.00	1.01	1.02	1.00	0.92	1.03
Molar A/NK	1.22	1.30	1.24	1.23	1.19	1.13	1.10	1.14	1.13	1.21
FeO <sub>t</sub> /MgO	4.42	5.69	4.61	5.85	10.98	18.85	30.85	10.28	2.77	12.52
Fe <sup>#</sup>	0.82	0.85	0.82	0.85	0.92	0.95	0.97	0.91	0.73	0.93
TiO <sub>2</sub> + FeO <sub>t</sub> + MgO	1.38	1.92	1.61	1.57	1.28	0.92	0.98	1.03	1.71	1.33
(Al <sub>2</sub> O <sub>3</sub> + CaO) / (FeO <sub>t</sub> + Na <sub>2</sub> O + K <sub>2</sub> O)	1.46	1.47	1.46	1.44	1.49	1.47	1.36	1.39	1.42	1.50
100 * [(MgO + FeO <sub>t</sub> + TiO <sub>2</sub> ) / SiO <sub>2</sub> ]	1.82	2.59	2.14	2.08	1.70	1.21	1.27	1.37	2.36	1.75
<i>Trace elements (ppm)</i>										
La	42.60	55.91	46.20	49.64	35.72	32.06	28.58	35.49	28.61	35.15
Ce	75.19	86.90	76.86	81.98	70.39	60.59	54.59	67.75	56.60	70.14
Pr	8.11	10.19	8.90	9.49	7.11	6.49	5.78	6.68	6.52	7.02
Nd	27.90	33.75	30.42	33.19	24.73	22.07	20.05	22.92	23.37	24.10
Sm	5.43	6.07	5.82	6.22	4.68	4.30	3.72	4.19	4.98	4.61
Eu	0.84	0.97	0.94	1.07	0.70	0.64	0.55	0.63	0.88	0.67
Gd	5.09	4.86	5.28	6.17	4.19	3.93	3.14	3.69	4.95	4.00
Tb	0.80	0.74	0.85	0.96	0.68	0.62	0.47	0.59	0.85	0.67
Dy	4.93	4.33	5.24	5.99	4.28	3.86	2.84	3.70	5.64	4.06
Ho	1.00	0.85	1.07	1.18	0.87	0.78	0.55	0.75	1.19	0.83
Er	3.02	2.63	3.04	3.46	2.53	2.27	1.65	2.32	3.62	2.50
Tm	0.49	0.42	0.49	0.55	0.41	0.37	0.28	0.38	0.59	0.39
Yb	3.24	2.84	3.25	3.45	2.84	2.45	1.96	2.55	4.03	2.55
Lu	0.49	0.43	0.49	0.54	0.43	0.39	0.31	0.40	0.63	0.38
Y	32.59	26.85	33.63	39.78	27.11	23.29	16.63	23.65	36.04	25.88
Rb	172.51	182.78	165.93	172.66	203.35	157.49	176.03	221.55	164.50	190.04
Ba	553.08	689.95	604.65	571.39	928.14	905.94	1022.8	984.18	689.25	879.01
Th	19.94	19.47	19.15	18.98	18.45	17.20	15.94	18.44	31.83	17.70
U	3.40	3.05	3.54	3.28	4.40	4.05	3.74	4.71	6.51	4.06
Nb	21.15	20.13	19.55	20.57	15.58	15.09	14.86	15.31	24.27	14.51
Ta	1.64	1.44	1.44	1.54	1.42	1.44	1.37	1.42	2.01	1.41
Sr	60.47	120.92	57.95	64.81	95.89	94.89	73.78	102.93	132.02	88.10
Hf	3.47	4.30	3.66	3.54	4.02	3.80	3.76	3.72	5.87	3.42
Ga	12.10	12.94	13.47	12.64	14.35	13.05	10.81	14.04	14.66	12.75
Zr	108.39	154.73	124.39	111.27	129.00	121.93	123.13	121.02	211.92	104.38
Pb	13.17	27.94	11.94	14.77	37.32	23.63	43.23	27.00	16.45	42.63
ΣREE	179.14	210.89	188.84	203.89	159.57	140.82	124.46	152.05	142.47	157.08
(La/Yb) <sub>N</sub>	9.43	14.12	10.20	10.33	9.01	9.40	10.44	9.97	5.09	9.90
δEu	0.48	0.53	0.51	0.52	0.47	0.47	0.48	0.48	0.54	0.47
δCe	0.93	0.83	0.87	0.87	1.02	0.97	0.98	1.01	0.98	1.03
10000 * Ga/Al	1.78	1.78	1.93	1.83	2.14	1.96	1.67	2.08	2.08	1.93
Nb + Y	1.41	1.36	1.38	1.39	1.49	1.44	1.46	1.49	1.51	1.50
Zr + Nb + Ce + Y	237.32	288.61	254.43	253.60	242.08	220.91	209.20	227.73	328.82	214.91

FeO<sub>t</sub>: total FeO.

observation was performed using an Olympus BX51 polarizing microscope. Cathodoluminescence (CL) observation and imaging were performed using a Gatan MonoCL4+ detector attached to a scanning electron microscope (FEI Quanta 450 FEG).

Zircon U-Pb and Lu-Hf isotope analyses were performed using an Agilent 7500a and Neptune ICP-MS with a GeoLas 2005 laser ablation system, with spot diameters of 32 μm and 44 μm. The carrier gas was Helium. Zircon 91500, the external standard for the U-Pb and Lu-Hf isotope analyses, was analyzed twice for every seven unknown analyses.

The isotope analyses results were constructed with ICPMSDataCal8.0 (Liu et al., 2010). Concordia diagrams and weighted mean plots of the U-Pb data were processed using ISOPLOT/Ex\_ver4 (Ludwig, 2003).

The mineral separation work was carried out at the Hebei Geological Survey Institute, China. (Cross-) polarized and CL observation and imaging and zircon U-Pb LA-ICP-MS analyses were conducted at the GPMR, CUG.

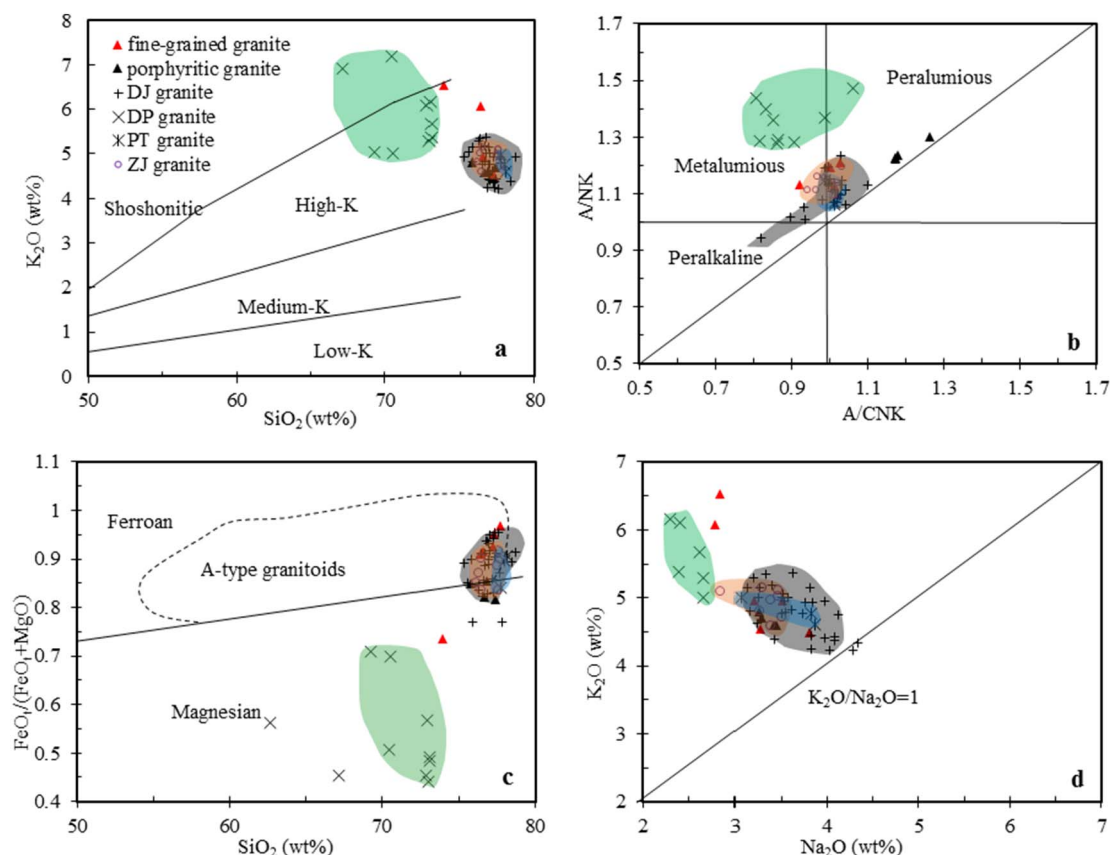


**Fig. 5.** Plots of (a)  $SiO_2$  versus  $K_2O$  (lines after Peccerillo and Taylor, 1976); (b)  $A/NK$  versus  $A/CNK$ ;  $A/NK = Al_2O_3 / (Na_2O + K_2O)$ ,  $A / CNK = Al_2O_3 / (CaO + Na_2O + K_2O)$  molecular ratio; (c)  $SiO_2$  versus  $FeO_t / (FeO_t + MgO)$  (lines after Frost et al., 2001a); and (d)  $Na_2O$  versus  $K_2O$  for the Luoyang granite. Data from DJ granite in Makeng Fe deposit area after Zhang et al. (2012c), Wang et al. (2015a) and Zhang et al. (2015b); data from DP granite in Dapai Fe deposit area after Yuan (2014); data from PT granite in Pantian Fe deposit area after Lai et al. (2014); date from ZJ granite in Zhongjia Fe deposit area after Niu et al. (unpublished data).

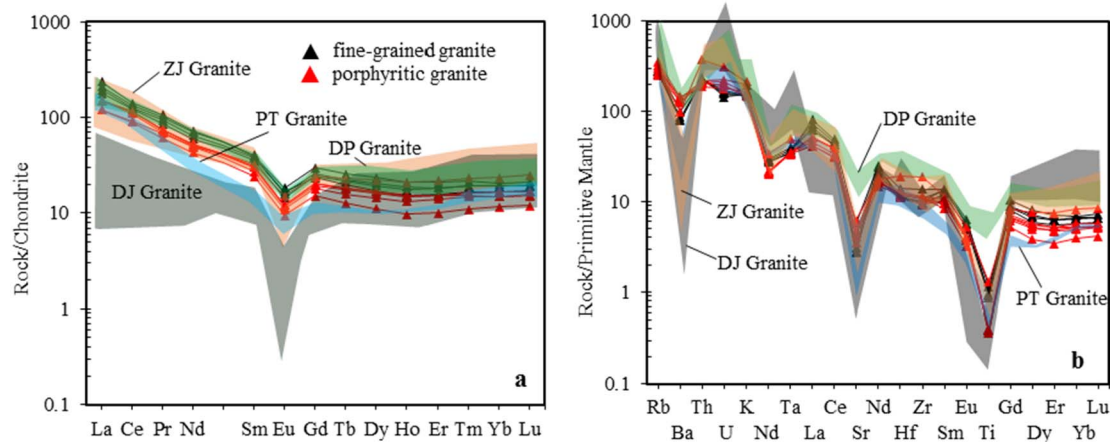


**Fig. 6.** Chondrite-normalized REE patterns (a) and primitive-mantle normalized spider diagrams (b) of the Luoyang granite. Normalizing values are from Sun and McDonough (1989). Data source of DJ, DP, PT and ZJ granites are same to Fig. 5.

#### 3.4. Granite Sr–Nd–Pb isotope analyses

The granite samples (G-1, G-3, G-8, and G-9; 200 mesh) were spiked with mixed isotope tracers and dissolved by a multistage acid procedure involving a concentrated  $HNO_3$ – $HCl$ – $HF$  acid mixture in Teflon capsules. To separate the matrix digests the Ion exchange chromatography was used.

The analyses of Rb–Sr, Sm–Nd, and Pb isotope concentrations and isotopic ratios were carried out using a TRITON (Thermo Scientific, Germany) thermal ionization mass spectrometer (TIMS), with internal

standardization and external calibration using bracketing isotope standard reference materials (SRMs). All chemical separation processes and isotopic analyses were performed in the Isotope Geochemistry Laboratory, Wuhan Center of Geological Survey, China.

#### 4. Analytical results

##### 4.1. Granite major and trace elements

The results of the Luoyang granite major and trace element analyses

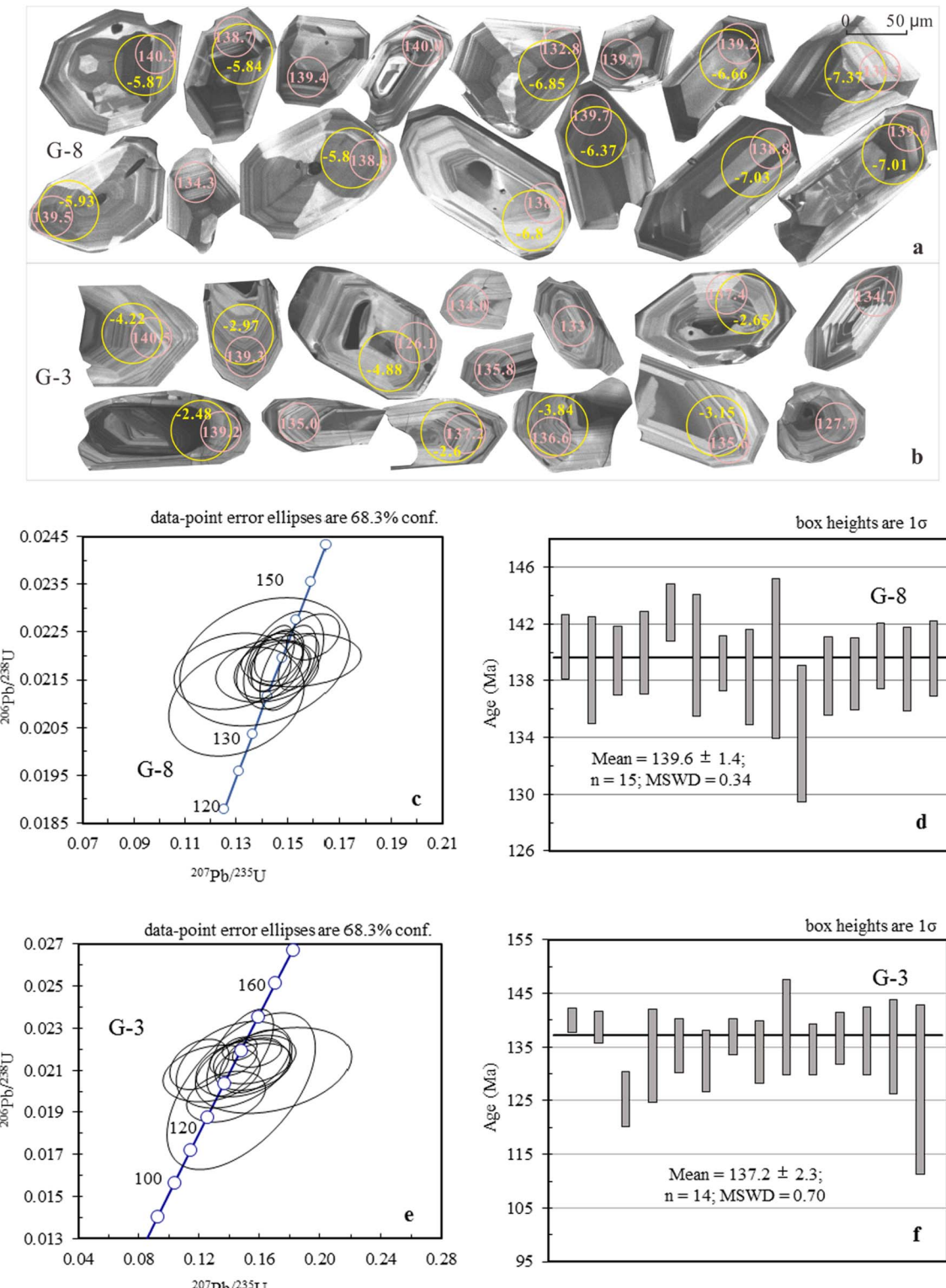


**Fig. 7.** Cathodoluminescence images, LA-ICP-MS U-Pb concordant diagrams and histogram plots for zircon ages from fine-grained granite (a, c and d) and porphyritic granite (b, e and f) in the Luoyang granitic pluton. The U-Pb dating spots are denoted by pink circles while the Lu-Hf analysis spots by yellow circles.

are summarized in Table 1. All samples with loss on ignition (LOI) < 2 wt% are relatively fresh and unaltered.

The results show high contents of  $\text{SiO}_2$ , from 72.45 to 76.86 wt% (mean = 75.29 wt%),  $\text{Na}_2\text{O} + \text{K}_2\text{O}$  of 7.68–9.20 wt% (mean = 8.17 wt%), and  $\text{Al}_2\text{O}_3$  of 12.11–13.48 wt% (mean = 12.67 wt%). The samples all plot within the high-K calc-alkaline field on a  $\text{K}_2\text{O}$  vs.  $\text{SiO}_2$  diagram (Fig. 5a), and exhibit metaluminous to peraluminous characteristics on

the A/NK (molar  $\text{Al}_2\text{O}_3 / (\text{Na}_2\text{O} + \text{K}_2\text{O})$ ) vs. A/CNK (molar  $\text{Al}_2\text{O}_3 / (\text{CaO} + \text{Na}_2\text{O} + \text{K}_2\text{O})$ ) diagram (Fig. 5b). They have high  $\text{Fe}^\#$  values ( $\text{FeO}_t / [\text{FeO}_t + \text{MgO}] = 0.73\text{--}0.97$ ; mean = 0.87; Fig. 5c) and  $\text{K}_2\text{O}/\text{Na}_2\text{O}$  ratios (1.18–2.30; mean = 1.56; Fig. 5d), but low contents of  $\text{MgO}$  (0.03–0.38 wt%; mean = 0.16 wt%),  $\text{TiO}_2$  (0.08–0.28 wt%; mean = 0.16 wt%), and  $\text{P}_2\text{O}_5$  (0.02–0.07 wt%; mean = 0.035 wt%).

The total REEs ( $\Sigma\text{REEs}$ ) are 124.46–210.89 ppm (mean = 165.92 ppm).

**Table 2**

LA-ICP-MS zircon U-Pb data for fine-grained granite (G-8) and porphyritic granite (G-3) from the Luoyang granite.

Sample	Total Pb	Th	U	Ratios of isotopes					Corrected age (Ma)				
	(ppm)	(ppm)	(ppm)	$^{207}\text{Pb}/^{206}\text{Pb}$	1σ	$^{207}\text{Pb}/^{235}\text{U}$	1σ	$^{206}\text{Pb}/^{238}\text{U}$	1σ	$^{207}\text{Pb}/^{235}\text{U}$	1σ	$^{206}\text{Pb}/^{238}\text{U}$	1σ
G-8-1	21.59	378.87	501.91	0.0484	0.0021	0.1467	0.0064	0.0220	0.0004	139.0	5.6	140.3	2.3
G-8-2	80.87	2077.63	1384.95	0.0502	0.0022	0.1502	0.0073	0.0218	0.0006	142.1	6.4	138.7	3.7
G-8-3	35.29	820.20	706.13	0.0514	0.0016	0.1543	0.0052	0.0219	0.0004	145.7	4.6	139.4	2.4
G-8-4	73.14	1885.04	1329.33	0.0475	0.0014	0.1443	0.0056	0.0219	0.0005	136.8	5.0	140.0	2.9
G-8-5	20.46	453.11	410.19	0.0524	0.0023	0.1598	0.0068	0.0224	0.0003	150.5	5.9	142.8	2.0
G-8-6	27.33	503.94	530.35	0.0490	0.0031	0.1485	0.0103	0.0219	0.0007	140.6	9.1	139.7	4.3
G-8-7	38.10	761.97	779.59	0.0489	0.0026	0.1472	0.0078	0.0218	0.0003	139.4	6.9	139.2	1.9
G-8-8	10.12	198.81	191.91	0.0442	0.0049	0.1285	0.0151	0.0217	0.0005	122.8	13.6	138.3	3.3
G-8-9	28.23	578.63	537.89	0.0466	0.0057	0.1410	0.0218	0.0219	0.0009	133.9	19.4	139.5	5.6
G-8-10	36.22	748.37	697.21	0.0460	0.0046	0.1300	0.0174	0.0210	0.0008	124.1	15.7	134.3	4.8
G-8-11	21.20	339.86	464.36	0.0479	0.0039	0.1420	0.0132	0.0217	0.0004	134.9	11.8	138.3	2.7
G-8-12	64.55	1598.37	1107.04	0.0479	0.0024	0.1438	0.0097	0.0217	0.0004	136.5	8.6	138.5	2.5
G-8-13	38.56	867.69	785.13	0.0503	0.0042	0.1551	0.0153	0.0219	0.0004	146.4	13.5	139.7	2.3
G-8-14	28.33	543.05	587.12	0.0479	0.0026	0.1430	0.0086	0.0218	0.0005	135.8	7.6	138.8	3.0
G-8-15	49.82	1193.79	854.72	0.0483	0.0024	0.1453	0.0071	0.0219	0.0004	137.7	6.3	139.6	2.6
G-3-1	29.36	731.62	562.95	0.0485	0.0026	0.1469	0.0076	0.0220	0.0004	139.1	6.7	140.5	2.3
G-3-2	12.56	276.45	264.13	0.0529	0.0037	0.1585	0.0108	0.0218	0.0005	149.4	9.4	139.3	2.9
G-3-3	14.80	394.94	321.02	0.0504	0.0063	0.1379	0.0173	0.0197	0.0008	131.1	15.4	126.1	5.0
G-3-4	15.82	491.79	277.04	0.0577	0.0075	0.1691	0.0340	0.0210	0.0013	158.6	29.6	134.0	8.5
G-3-5	16.62	575.07	255.45	0.0429	0.0056	0.1202	0.0130	0.0213	0.0008	115.3	11.8	135.8	5.0
G-3-6	10.69	270.26	235.39	0.0448	0.0069	0.1282	0.0213	0.0209	0.0009	122.5	19.1	133.0	5.6
G-3-7	12.41	312.09	250.10	0.0488	0.0039	0.1426	0.0104	0.0215	0.0005	135.4	9.2	137.4	3.3
G-3-8	11.66	291.01	209.07	0.0526	0.0075	0.1492	0.0206	0.0211	0.0009	141.2	18.2	134.7	5.7
G-3-9	15.21	501.26	247.36	0.0539	0.0069	0.1472	0.0146	0.0218	0.0014	139.4	12.9	139.2	8.6
G-3-10	13.44	364.61	225.88	0.0532	0.0058	0.1560	0.0168	0.0212	0.0007	147.2	14.8	135.0	4.7
G-3-11	13.77	357.02	258.48	0.0555	0.0065	0.1569	0.0181	0.0215	0.0008	148.0	15.9	137.2	4.8
G-3-12	10.71	267.07	187.14	0.0557	0.0061	0.1569	0.0154	0.0214	0.0010	148.0	13.5	136.6	6.2
G-3-13	12.43	372.30	229.43	0.0483	0.0093	0.1432	0.0254	0.0213	0.0014	135.9	22.5	135.6	8.6
G-3-14	12.78	396.28	290.11	0.0542	0.0124	0.1479	0.0325	0.0200	0.0025	140.1	28.7	127.7	15.5

**Table 3**

LA-ICP-MS zircon Hf data for the Luoyang granite.

Sample	$t$ (Ma)	$^{176}\text{Hf}/^{177}\text{Hf}$	1σ	$^{176}\text{Lu}/^{177}\text{Hf}$	$^{176}\text{Yb}/^{177}\text{Hf}$	$\varepsilon_{\text{Hf}}(0)$	$\varepsilon_{\text{Hf}}(t)$	2σ	$T(\text{Hf})_{\text{DM1}}$ (Ma)	$T(\text{Hf})_{\text{DM2}}$ (Ma)	$f_{\text{Lu/Hf}}$
G-8-1	140.3	0.282523	0.000011	0.001693	0.042912	-8.79	-5.87	0.66	1050	1386	-0.95
G-8-2	138.7	0.282526	0.000015	0.002207	0.054406	-8.68	-5.84	0.75	1060	1383	-0.93
G-8-7	139.2	0.282497	0.000015	0.001970	0.050037	-9.72	-6.85	0.75	1096	1439	-0.94
G-8-5	142.8	0.282499	0.000011	0.001343	0.033151	-9.66	-6.66	0.66	1075	1431	-0.96
G-8-8	138.3	0.282480	0.000011	0.000683	0.015990	-10.34	-7.37	0.66	1083	1467	-0.98
G-8-9	139.5	0.282524	0.000014	0.002404	0.058803	-8.77	-5.93	0.72	1070	1388	-0.93
G-8-11	138.3	0.282528	0.000013	0.002050	0.049195	-8.64	-5.80	0.71	1054	1380	-0.94
G-8-12	138.5	0.282499	0.000012	0.001984	0.048262	-9.65	-6.80	0.67	1093	1435	-0.94
G-8-13	139.7	0.282511	0.000013	0.002115	0.051415	-9.24	-6.37	0.69	1080	1413	-0.94
G-8-14	138.8	0.282492	0.000014	0.002023	0.048442	-9.89	-7.03	0.72	1104	1448	-0.94
G-8-15	139.6	0.282492	0.000014	0.001723	0.041887	-9.91	-7.01	0.73	1096	1448	-0.95
G-3-1	140.5	0.282568	0.000012	0.000794	0.019056	-7.23	-4.22	0.67	963	1294	-0.98
G-3-2	139.3	0.282605	0.000010	0.001375	0.030911	-5.90	-2.97	0.63	925	1224	-0.96
G-3-3	126	0.282558	0.000013	0.000920	0.021699	-7.57	-4.88	0.70	980	1320	-0.97
G-3-7	137.4	0.282616	0.000015	0.001804	0.043834	-5.50	-2.65	0.74	919	1205	-0.95
G-3-9	139.2	0.282620	0.000016	0.001767	0.042101	-5.38	-2.48	0.77	913	1197	-0.95
G-3-11	137.2	0.282617	0.000012	0.001396	0.033240	-5.48	-2.60	0.66	909	1202	-0.96
G-3-12	136.6	0.282581	0.000011	0.001010	0.024032	-6.75	-3.84	0.65	950	1270	-0.97
G-3-13	135.6	0.282603	0.000014	0.001769	0.044309	-5.97	-3.15	0.73	937	1231	-0.95

 $^{176}\text{Lu}/^{177}\text{Hf}$ ,  $^{176}\text{Hf}/^{177}\text{Hf}$  ratios of DM (depleted mantle) are 0.0384 and 0.28325;  $^{176}\text{Lu}/^{177}\text{Hf}$  ratios of crust are 0.015;  $\lambda^{176}\text{Lu} = 0.1867 \times 10^{-10}/\text{year}$ .

Chondrite-normalized REE patterns (Fig. 6a) invariably show light REE (LREE) enrichment and negative Eu anomalies, with  $(\text{La/Yb})_N = 5.09\text{--}14.12$  (mean = 9.79) and  $\delta\text{Eu} = 0.47\text{--}0.54$  (mean = 0.49; Table 1). The primitive mantle-normalized spider diagram shows prominent negative anomalies for Ba, Nb, Sr, Eu, and Ti, and positive anomalies for Rb, Th, and U in the granites (Fig. 6b).

#### 4.2. Zircon U-Pb dating

The polarizing microscope revealed no obvious evidence of inclusions or inheritance in zircon grains in the fine-grained granite sample (G-8) and porphyritic granite sample (G-3). In addition, these zircon

grains show euhedral-subhedral in shape and are colorless, with length/width ratios of 1:1 to 5:1 and well-defined oscillatory zoning in CL images (Fig. 7a and b). The morphologies and internal structures suggest that these zircons are igneous origin.

Fifteen spot analyses from porphyritic granite sample (G-3) were obtained and the results are listed in Table 2. The U and Th contents and Th/U ratios of zircons in the porphyritic granite vary from 192 to 1385 ppm, 199 to 2078 ppm, and 0.73 to 1.50, respectively. Grains, with  $^{206}\text{Pb}/^{238}\text{U}$  ages vary from 134.3 to 142.8 Ma, and yield a weighted average  $^{206}\text{Pb}/^{238}\text{U}$  age of  $137.2 \pm 2.3$  Ma ( $1\sigma$ , mean square weighted deviation (MSWD) = 0.70, n = 15; Fig. 7c-d).

Fourteen spot analyses from fine-grained granite sample (G-8) were

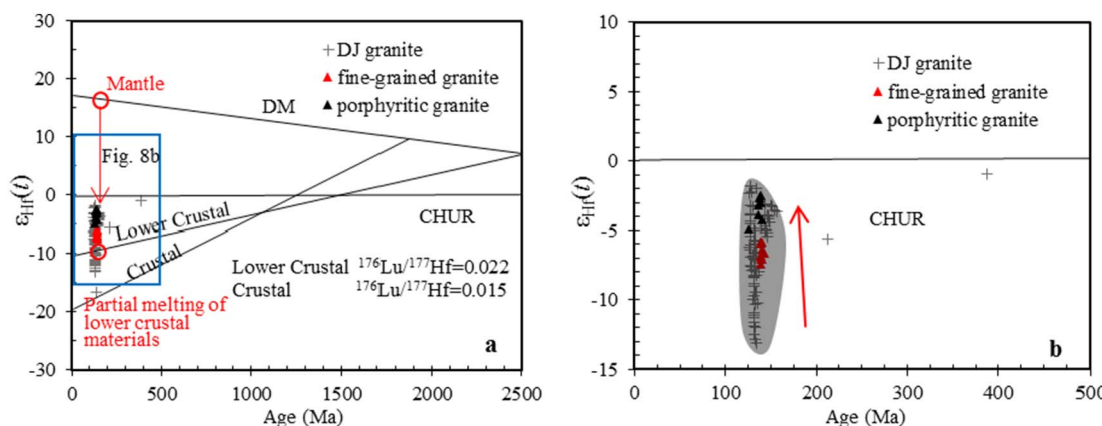


**Fig. 8.** Hf isotope evolution diagram. The DM line denotes the evolution of depleted mantle with a present-day  $^{176}\text{Hf}/^{177}\text{Hf} = 0.28325$  and  $^{176}\text{Lu}/^{177}\text{Hf} = 0.0384$  (Griffin et al., 2000) and the corresponding lines of crustal extraction are calculated by assuming a  $^{176}\text{Lu}/^{177}\text{Hf}$  ratio of 0.015 for the average continental crust (after Wong et al., 2009) and a ratio of 0.022 for the average lower crustal (after Amelin et al., 1999). Hf isotopic data of DJ granite is from Zhang et al. (2012a) and Wang et al. (2015a).

obtained and the results are listed in Table 2. The U and Th contents and Th/U ratios of zircons in the porphyritic granite vary from 187 to 563 ppm, 267 to 732 ppm, and 1.05 to 2.25, respectively. Grains, with  $^{206}\text{Pb}/^{238}\text{U}$  ages vary from 126.1 to 140.5 Ma, and yield a weighted average  $^{206}\text{Pb}/^{238}\text{U}$  age of  $139.6 \pm 1.4$  Ma ( $1\sigma$ , MSWD = 0.34,  $n = 14$ ; Fig. 7e-f).

The relatively high Th/U ratios also suggest that these zircons are igneous origin. All data points are credible and concordant at the  $2\sigma$  level; all are symmetrically distributed on both sides of the concordia diagram (Fig. 7c-f).

#### 4.3. Zircon Hf isotopes

The LA-ICP-MS Lu-Hf analytical results are listed in Table 3. Eleven spot analyses of Lu-Hf isotopes were obtained for the fine-grained granite (G-8), yielding  $\epsilon_{\text{Hf}}(t)$  values between  $-7.37$  and  $-5.80$  (mean =  $-6.50$ ; Fig. 8), corresponding to two-stage Hf model ages ( $T(\text{Hf})_{\text{DM2}}$ ) model ages between 1.38 Ga and 1.47 Ga (mean = 1.42 Ga). Eight spot analyses were made for the porphyritic granite (G-3), giving  $\epsilon_{\text{Hf}}(t)$  values between  $-4.88$  and  $-2.48$  (mean =  $-3.35$ ) (Fig. 8), corresponding to  $T(\text{Hf})_{\text{DM2}}$  model ages between 1.20 Ga and 1.32 Ga (mean = 1.24 Ga).

#### 4.4. Granite Sr-Nd-Pb isotopes

The results of the Sr-Nd-Pb isotope analyses are summarized in Table 4 and Fig. 9. The Sr, Nd, and Pb isotope ratios at 137 Ma (samples G-1 and G-3) and 140 Ma (samples G-8 and G-9) were calculated and reported as initial  $^{87}\text{Sr}/^{86}\text{Sr}$  ( $I_{\text{Sr}}$ ),  $\epsilon_{\text{Sr}}(t)$ ,  $\epsilon_{\text{Nd}}(t)$ , initial  $^{208}\text{Pb}/^{204}\text{Pb}$  ( $(^{208}\text{Pb}/^{204}\text{Pb})_i$ ), initial  $^{207}\text{Pb}/^{204}\text{Pb}$  ( $(^{207}\text{Pb}/^{204}\text{Pb})_i$ ), and initial  $^{206}\text{Pb}/^{204}\text{Pb}$  ( $(^{206}\text{Pb}/^{204}\text{Pb})_i$ ).

The fine-grained granite and porphyritic granite have similar Sr-Nd isotopic characteristics, with low  $I_{\text{Sr}}$  ratios (0.704931–0.706213), relatively high  $\epsilon_{\text{Nd}}(t)$  values ( $-5.27$  to  $-4.85$ ) and two-stage Nd isotopic model ages from 1.33 to 1.36 Ga. The Pb isotope is also consistent between the two granite types. The  $(^{206}\text{Pb}/^{204}\text{Pb})_i$ ,  $(^{207}\text{Pb}/^{204}\text{Pb})_i$  and  $(^{208}\text{Pb}/^{204}\text{Pb})_i$  ratios vary from 18.382721 to 18.709090, from 15.664929 to 15.753257, and from 38.507267 to 39.208348, respectively.

## 5. Discussion

### 5.1. Mineralization age

Yuan et al. (2013) and Zhao et al. (2016) showed that the crystallization ages of mineralization related granite in the Dapai deposit are

$132.4 \pm 0.8$  Ma and  $127.0 \pm 1.8$  Ma, and the molybdenite Re-Os ages are  $131.6 (\pm 2.1)$ – $135.2 (\pm 2.4)$  Ma and  $131.1 (\pm 2.2)$ – $133.7 (\pm 1.9)$  Ma. They exhibited multistage intrusive and mineralization processes. In addition, the zircon U-Pb dating on the DJ granitic pluton has proved that the pluton had different crystallization ages of between 125 and 145 Ma. The molybdenite Re-Os ages in the Makeng deposit range from  $131.9 (\pm 1.9)$  Ma to  $133.3 (\pm 2.3)$  Ma, whereas the garnet-magnetite Sm-Nd ages indicate the extensive magnetite mineralization and skarn alteration occurred intensively around  $157 \pm 15$  Ma (Zhang et al., 2012b; Zhang et al., 2015b). It also suggests multistage granite emplacement and mineralization (Zhang et al., 2015b).

Zhang et al. (2012d) have reported zircon U-Pb ages of  $131.6 (\pm 0.6)$  Ma and  $131 (\pm 1)$  Ma for the fine-grained granite and porphyritic granite, and propose the mineralization age of  $133 (\pm 1.9)$  to  $134 (\pm 4.2)$  Ma according to three molybdenite, syngenetic with magnetite in the Luoyang Fe deposit; and Re-Os ages of  $133 (\pm 1.9)$  Ma,  $133.1 (\pm 2.3)$  Ma and  $134 (\pm 4.2)$  Ma. The zircon U-Pb dating in this work suggested that the fine-grained granitic stock in the bottom of the deposit was emplaced at  $139.6 (\pm 1.4)$  Ma, and the later porphyritic granite intruded at  $137.2 (\pm 2.3)$  Ma (Fig. 7).

The crystallization of molybdenite is relatively later than the magnetite in the skarn deposit and the deviation in molybdenite Re-Os ages is reached at 4.2 Ma, almost the lower limit of the new U-Pb ages of the Luoyang granite in this work. Therefore, although these new zircon U-Pb ages are not wholly consistent with the Re-Os age, it remains credible that the deposit was related to the late Yanshanian granite, and might represent the same multistage emplacement as that of the DJ granite in the Makeng deposit and the DP granite in the Dapai deposit (Zhang et al., 2015b).

### 5.2. Properties of the Luoyang granite

According to the nature of the protolith, granites have commonly been divided into I-, S-, M- and A-types (Pitcher, 1982). The results show that the Luoyang granite are similar to the DJ granite in the Makeng deposit, the DP granite in the Dapai deposit, the PT granite in the Pantian deposit, and the ZJ granite in the Zhongjia deposit. They are metaluminous to weakly peraluminous, with  $\text{P}_2\text{O}_5$  and Pb negatively and positively correlated with  $\text{SiO}_2$ , respectively (Fig. 10). In addition, Y and Th in the granites display obvious positive correlations with Rb (Fig. 10). Combined with the Sr isotopic data, it is clear that the Luoyang granite is not characteristic of an S-type granite, but rather can be classified as I- or A-type. The absence of muscovite and garnet also indicate the Luoyang granite is not an S-type granite.

The Luoyang, PT, and ZJ granites exhibit geochemical

**Table 4**  
Sr, Nd, and Pb isotopic data for the Luoyang granite.

Sample	<i>t</i> (Ma)	$^{206}\text{Pb}/^{204}\text{Pb}$	$^{207}\text{Pb}/^{204}\text{Pb}$	$^{208}\text{Pb}/^{204}\text{Pb}$	Pb (ppm)	Th (ppm)	U (ppm)	$(^{206}\text{Pb}/^{204}\text{Pb})_{\text{i}}$	$(^{207}\text{Pb}/^{204}\text{Pb})_{\text{i}}$	$(^{208}\text{Pb}/^{204}\text{Pb})_{\text{i}}$	$\Delta\alpha$	$\Delta\beta$	$\Delta\gamma$
LY-G-1	137	19.045	15.736	39.773	13.2	19.9	3.4	18.683451	15.718356	39.035658	108	27	66
LY-G-3	137	18.794	15.685	39.235	11.9	19.2	3.5	18.382721	15.664429	38.507267	93	23	53
LY-G-8	140	18.958	15.703	39.527	27	18.4	4.7	18.70909	15.690637	39.208346	103	25	61
LY-G-9	140	19.024	15.781	39.781	16.5	31.8	6.5	18.456232	15.753527	38.873509	107	30	68
DP-G-1 <sup>b</sup>	134	18.943	15.693	39.31	15.9	14.3	2.4	18.734937	15.682859	38.909562	102	24	55
DP-G-3 <sup>b</sup>	134	18.684	15.727	39.283	29.5	18.6	2.4	18.573224	15.721601	39.003431	87	26	54
DP-G-5 <sup>b</sup>	134	18.92	15.719	39.514	10.9	16.5	2.4	18.61374	15.704073	38.836569	100	26	60
DP-G-4 <sup>b</sup>	134	18.689	15.715	39.175	40.7	26.8	4.1	18.552114	15.708328	38.882997	87	25	51
DY02 <sup>a</sup>	133	18.995	15.673	39.184	21.4	16.9	5.16	18.669872	15.657116	38.835523	105	23	52
DY05 <sup>a</sup>	133	19.028	15.673	39.158	45.9	35.4	14.4	18.604933	15.652389	38.817645	107	23	51
DY06 <sup>a</sup>	133	19.154	15.671	39.413	26.4	31.9	7.27	18.780765	15.652817	38.877053	114	23	58
DY07 <sup>a</sup>	133	19.018	15.692	39.202	40.8	28.7	8.71	18.729913	15.677965	38.891335	106	24	52
DY08 <sup>a</sup>	144	18.787	15.67	39.187	33.8	25.9	6.74	18.49644	15.655778	38.821822	94	23	52
Sample		Rb (ppm)	Sr (ppm)	$^{87}\text{Sr}/^{86}\text{Sr}$	$I_{\text{Sr}}$	$\epsilon_{\text{Sr}}(t)$	Sm (ppm)	Nd (ppm)	$^{147}\text{Sm}/^{144}\text{Nd}$	T(Nd)Dm2 (Ma)	$\epsilon_{\text{Nd}}(t)$		
LY-G-1	162.2	61.7	7.587	0.71995	0.705176	11.88	5.39	28.48	0.1145	0.512294	1317	1360	-5.27
LY-G-3	174.7	118.2	4.266	0.71452	0.706213	26.6	5.78	33.50	0.1044	0.512285	1208	1360	-5.27
LY-G-8	155.9	58.9	7.633	0.72012	0.704931	8.45	5.77	31.08	0.1124	0.512312	1262	1328	-4.85
LY-G-9	157.1	64.9	6.990	0.71894	0.70503	9.86	6.13	32.61	0.1137	0.512293	1308	1360	-5.25
DP-G-1 <sup>b</sup>	313.4	158.4	5.711	0.7187	0.707823	201.56	4.51	18.37	0.1485	0.51231	1963	1379	-5.58
DP-G-3 <sup>b</sup>	291.8	141.3	5.961	0.71926	0.707907	209.51	4.26	17.79	0.1449	0.512317	1845	1364	-5.38
DP-G-5 <sup>b</sup>	292.2	143.8	5.865	0.71903	0.707859	206.25	4.47	18.93	0.1429	0.512308	1812	1375	-5.52
DP-G-4 <sup>b</sup>	305.9	153.8	5.742	0.71873	0.707794	201.99	5.54	24.29	0.1381	0.512327	1660	1339	-5.07
DY02 <sup>a</sup>	221	44.7	14.327	0.740568	0.713485	129.79	5.50	14.60	0.2274	0.512263	1620	-7.84	
DY05 <sup>a</sup>	367	43.6	24.334	0.755542	0.709541	73.78	7.83	27.00	0.1754	0.512225	3662	1543	-7.70
DY06 <sup>a</sup>	298	28.1	30.659	0.766743	0.708785	63.06	2.89	12.20	0.1429	0.512223	1994	1509	-7.18
DY07 <sup>a</sup>	398	57.3	20.123	0.75001	0.711969	108.27	7.63	26.60	0.1732	0.512224	3469	1543	-7.68
DY08 <sup>a</sup>	275	89.8	8.872	0.729052	0.710891	93.15	8.66	41.40	0.1266	0.51213	1784	1636	-8.62

$\Delta\alpha = [\alpha_{\text{M}}(t) - 1] \times 1000$ ,  $\Delta\beta = [B/\beta_{\text{M}}(t) - 1] \times 1000$ . Where,  $\alpha$ ,  $\beta$ , and  $\gamma$  are the actual measurement values of  $^{206}\text{Pb}/^{204}\text{Pb}$ ,  $^{207}\text{Pb}/^{204}\text{Pb}$ , and  $^{208}\text{Pb}/^{204}\text{Pb}$ , whereas  $\alpha_{\text{M}}(t)$ ,  $\beta_{\text{M}}(t)$ , and  $\gamma_{\text{M}}(t)$  represent the mantle values of  $^{206}\text{Pb}/^{204}\text{Pb}$ ,  $^{207}\text{Pb}/^{204}\text{Pb}$ , and  $^{208}\text{Pb}/^{204}\text{Pb}$  in the time of  $t$ , respectively.  $^{147}\text{Sm}/^{144}\text{Nd}$ ,  $^{143}\text{Nd}/^{144}\text{Nd}$  ratios of present CHUR (chondritic uniform reservoir) are 0.1967 and 0.512638;  $^{87}\text{Rb}/^{86}\text{Sr}$  ratios of present UR (uniform reservoir) are 0.7045 and 0.0827;  $\lambda^{87}\text{Rb} = 1.42 \times 10^{-11}/\text{year}$ ,  $\lambda^{147}\text{Sm} = 6.5 \times 10^{-12}/\text{year}$ ;  $\lambda^{235}\text{U} = 9.8485 \times 10^{-10}/\text{year}$ ,  $\lambda^{232}\text{Th} = 4.9475 \times 10^{-11}/\text{year}$ ,  $a_0 = 9.307$ ,  $b_0 = 10.294$ ,  $C_0 = 29.476$ ,  $T = 4.23$  Ga.

<sup>a</sup> Isotope data for Dayang granites are from Zhang et al. (2012c).

<sup>b</sup> Isotope data for Dapai granites are from Zhang (unpublished data).

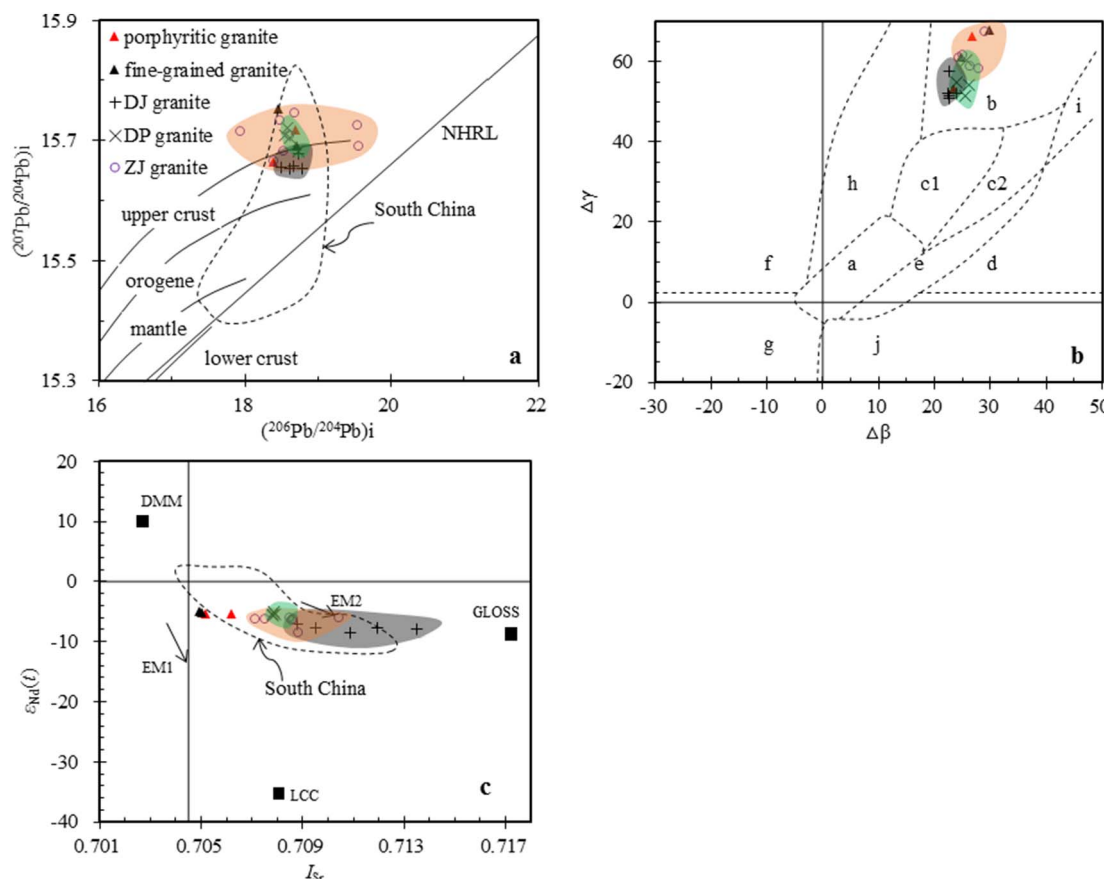


**Fig. 9.** Isotope composition of Pb (a, b) and plot of  $\varepsilon_{\text{Nd}}(t)$  versus  $I_{\text{Sr}}$  for Luoyang granites (c). Mantle, orogene, upper crust and lower crust lines are after Zartman and Doe (1981); the Northern Hemisphere reference line (NHRL) is from Hart (1984); fields of a-Mantle source, b-Upper crust source, c/Subduction belt source by mixing mantle with upper crust, c1-Magmatism source, c2-Sedimentation source, d-Chemical sedimentary source, e-Sea floor hydrothermal source, f-Mid-high grade metamorphism source, g-High-grade metamorphism (lower crust) source, h-Orogenic belt source, i-Paleoshale (upper crust) source and j-Retrograde metamorphism source are after Zhu (1998); data for LCC (model lower continental crust), GLOSS (Global subducting sediments) and DMM are from Jahn et al. (1999), Plank and Langmuir (1998) and Workman and Hart (2005), respectively; the trends for EM-I and EM-II are from Zindler and Hart (1986); South China (represented by rocks from the middle-lower Yangtze valley and the regions south of it) calculated back to  $t = 130$  Ma from Zhao and Zheng (2009). Data source of DP granite is from Zhang (unpublished data); data source of DJ and ZJ granite are same to Fig. 6.

characteristics of high  $\text{Na}_2\text{O} + \text{K}_2\text{O}$ ,  $\text{FeO}_t / \text{MgO}$ ,  $\text{Ga}/\text{Al}$ , and high field strength elements (HFSE); and low  $\text{Al}_2\text{O}_3$ ,  $\text{Sr}$ ,  $\text{Ti}$ ,  $\text{Ba}$ , and  $\text{Eu}$  values (Fig. 11a and b; Fig. 6), which is similar to A-type granites. They also show some geochemical characteristics of highly fractionated granites. In contrast, the DP granite exhibits unfractionated characteristics (Fig. 11a). This is also confirmed by the  $(\text{Al}_2\text{O}_3 + \text{CaO}) / (\text{FeO}_t + \text{Na}_2\text{O} + \text{K}_2\text{O})$  vs.  $100 * (\text{MgO} + \text{FeO}_t + \text{TiO}_2) / \text{SiO}_2$  diagram (Fig. 11c), which can effectively discriminate fractionated granites (Sylvester, 1989).

However, distinguishing the A-type and highly fractionated I-type granites remains challenging (White and Chappell, 1983; King et al., 1997, 2001). A-type granites are generally emplaced later than I-types granites (Wu et al., 2003). We therefore conclude that the Luoyang granite, along with the PT and ZJ granites, actually corresponds to a transitional-type between highly fractionated I-type and A-type granites; whereas, the DP granite exhibits unfractionated I-type characteristics and the DJ granite shows A-type characteristics.

The striking depletions in Ba, Sr, Nb, P, Ti, and Eu observed in spider diagrams (Fig. 6) show that advanced fractional crystallization occurred during the formation of these granites. Apatite separation would cause P depletion, whereas Ti-bearing phase (ilmenite, titanite, etc.) fractionation caused Nb-Ti depletion. Fractionation of plagioclase and/or K-feldspar produced negative Eu anomalies. The Sr-Eu depletion required the fractionation of plagioclase, and Ba-Eu depletion was related to K-feldspar separation. The fractionation of plagioclase occurred during the early stage of fractional crystallization, whereas K-

feldspar separated during later stages. This is reflected in the log-log diagram of Ba vs. Sr (Fig. 12a), where Sr concentration decreases sharply in the early stage of crystallization but changes little in the later stage, whereas the Ba concentration shows the opposite pattern. In the  $(\text{La}/\text{Yb})_N$  vs. La diagram (Fig. 12b), variations in REE contents appear to be in agreement with the fractionation of allanite and monazite and, to a lesser extent, apatite; whereas, titanite and zircon have not exerted obvious influence. Therefore, the major elements variations are mainly caused by the fractionation of K-feldspar and plagioclase, with Rb, Sr, and Ba abundances controlled by feldspars. In addition, the fractionation of monazite, allanite, and apatite controlled REE variations.

### 5.3. Petrogenesis

The Luoyang granite exhibits high  $\text{SiO}_2$  (> 72 wt%), but low  $\text{MgO}$  (< 0.4 wt%) contents; therefore, it is not derived directly from the mantle because rocks with mantle origin exhibit high Mg characteristics (Baker et al., 1995; Hirose, 1997). The lack of mafic enclaves in the Luoyang granite pluton together with the constant and horizontal trend of  $\varepsilon_{\text{Nd}}(t)$  values with increasing  $\text{SiO}_2$ , suggest that neither significant magma mixing nor crustal assimilation were important in its genesis (Fig. 13).

Partial melting is considered as an important mechanism for A-type granites genesis (Frost et al., 1999; Frost et al., 2001b; Dall'Agnol and de Oliveira, 2007; Wang et al., 2010). The characteristics of the Luoyang granite pluton, showing several A-type granite characteristics

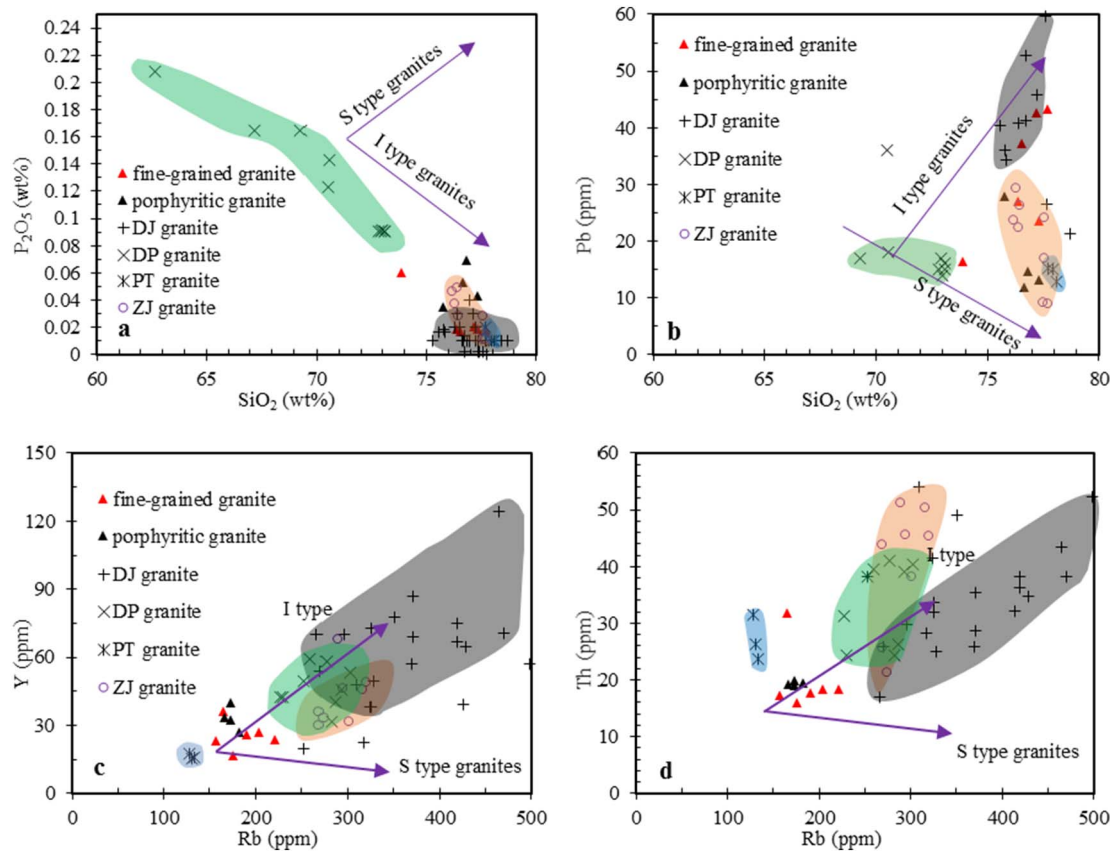


Fig. 10. Plot of  $P_2O_5$ , Pb, Y, and Th against Rb (after Chappell and White, 1992; Chappell, 1999). Data source of DJ, DP, PT and ZJ granites are same to Fig. 6.

as well as the high  $K_2O/Na_2O$  ratios (1.05–1.57; mean = 1.31), low  $TiO_2 + FeO_t + MgO$  contents (0.92–1.92 wt%; mean 1.37 wt%), high negative  $\epsilon_{Nd}(t)$  values (−5.27 to −4.85; mean = −5.16), Pb isotope compositions (Fig. 9a and b), and the lack of mafic enclaves suggest a crustal source.

The two-stage depleted mantle Nd model age ( $T(Nd)_{DM2}$ ) for the Luoyang granite is 1.28–1.36 Ga (mean = 1.35 Ga), younger than the Cathaysia metamorphic basement, with a  $T(Nd)_{DM2}$  peak at around 1.7–1.9 Ga (Gilder et al., 1996; Chen and Jahn, 1998; Shen et al., 2000), which indicates the involvement of mafic sources in the Paleoproterozoic crustal source. The relatively high  $\epsilon_{Nd}(t)$  values (−5.27 to −4.85; mean = −5.16; Fig. 9c) also suggest that some mafic sources were involved.

These highly fractionated I-type to A-type granites, contain abundant zircons with relatively high  $^{176}Hf/^{177}Hf$  ratios (0.28248–0.28262; mean = 0.28254) and  $\epsilon_{Hf}(t)$  values (−7.37 to −2.48; mean = −5.18), were generated with an involvement of juvenile mantle components (Li et al., 2014). On the  $t$ - $\epsilon_{Hf}(t)$  diagram (Fig. 8), the zircon samples from these granites plot primarily in the field between the lower crustal and CHUR reference lines. In addition, they show slightly younger ages  $T(Hf)_{DM2}$  (1.20–1.47 Ga; mean = 1.35 Ga), consistent with  $T(Nd)_{DM2}$  (1.28–1.36 Ga; average 1.35 Ga), and the eastern Cathaysia basement rocks ( $T(Hf)_{DM2}$  peak ~1.4 Ga; Xu et al., 2007). Therefore, we infer that some juvenile components from a depleted mantle source were involved in the Luoyang granite genesis. Furthermore, the  $\epsilon_{Hf}(t)$  values of porphyritic granite (−4.88 to −2.48; mean = −3.35;  $137.2 \pm 2.3$  Ma) are relatively higher than the  $\epsilon_{Hf}(t)$  values of fine-grained monzonitic granite (−7.37 to −5.80; mean = −6.50;  $139.6 \pm 1.4$  Ma), which indicates that more mafic sources were involved in the later process. This is a more reasonable explanation for the transformation of the granite, from highly fractionated I-type to A-type, in southwestern Fujian Province at

approximately 140 Ma.

Based on these results, we infer that the source magma of the Luoyang granite is coincident with the other Makeng-type skarn Fe deposits in southwestern Fujian Province. The magma was derived from partial melting of the Proterozoic Cathaysia metasedimentary basement, and involved some underplating of mafic magma in the depleted mantle and/or lower tholeiitic crust, which also provided the heat source for the partial melting (Zhang et al., 2015b).

#### 5.4. Tectonic implications

With the aim of obtaining a credible understanding of the geological environment, samples from the Luoyang granite are plotted on a tectonic discrimination diagram of Rb vs. Y + Nb (Fig. 14; Pearce et al., 1984). All the samples distribute in a field straddling the boundary between WPG (within-plate granites) and VAG (volcanic arc granites). However, different geological processes (e.g., partial melting of the subducted slab, mantle wedge subduction and enrichment, or fractional crystallization processes) affect the contents of REEs and other trace elements in igneous intrusions. Therefore, it is difficult to discriminate the tectonic setting based simply on the Rb vs. Y + Nb tectonic discrimination diagram. Additionally, tectonic determining diagrams of granites may reflect the tectonic setting of either their parental magmas or the protoliths (Li et al., 2014).

However, we can at least reduce ambiguity in geochemical tectonic discriminants via sufficient geological and geochemical evidence. The Luoyang granite is more characteristic of a highly fractionated I-type to A-type; whereas, the Makeng deposit DJ granite is characteristic of an A-type. A-type granites usually occur in extensional tectonic environments and have no causality relationship with the nature of the magma source (Whalen et al., 1987; Eby, 1992); therefore, the intrusion of the Luoyang highly fractionated I-type to A-type granite in southwestern

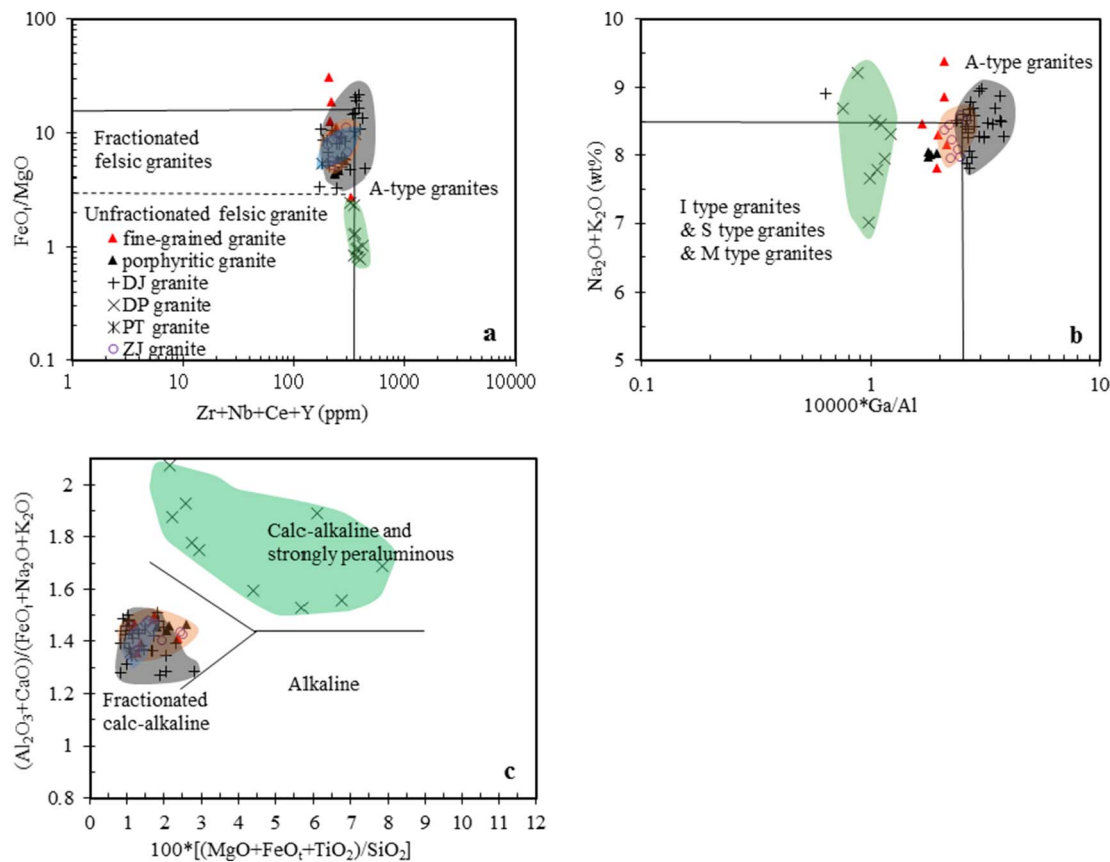


**Fig. 11.** Total FeO/MgO versus Zr + Nb + Ce + Y (a); (Na<sub>2</sub>O + K<sub>2</sub>O) versus 10000 \* Ga/Al (b); and (Al<sub>2</sub>O<sub>3</sub> + CaO) / (FeO<sub>t</sub> + Na<sub>2</sub>O + K<sub>2</sub>O) versus 100 \* [(MgO + FeO<sub>t</sub> + TiO<sub>2</sub>) / SiO<sub>2</sub>] (c) diagrams for the Luoyang granite. a and b diagrams after Whalen et al. (1987); c after Sylvester (1989). Data source of DJ, DP, PT and ZJ granites are same to Fig. 6.

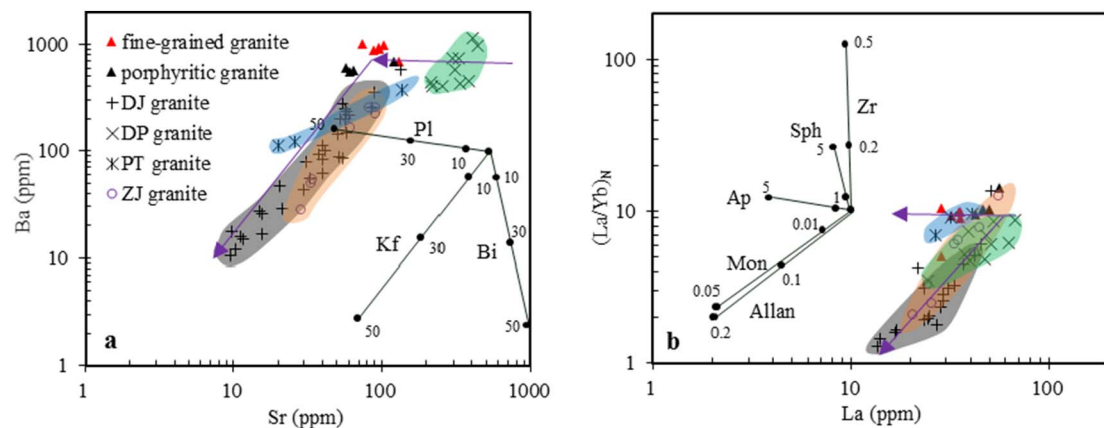


**Fig. 12.** Ba versus Sr (a) and (La/Yb)<sub>N</sub> versus La (b) diagrams for the Luoyang granite. Kfs, K-feldspar; Bt, biotite; Pl, plagioclase; Zr, zircon; Sph, Spheine; Ap, apatite; Mon, monazite; Allan, allanite. Element distribution coefficients are from Hanson (1978; Kfs), Icenhower and London (1995; Bt), Blundy and Shimizu (1991; Pl, 750°C, An50), Mahood and Hildreth (1983; Zr), Green and Pearson (1986; Sph), Arth (1976; Ap), Yurimoto et al. (1990; Mon) and Green et al. (1989; Allan). Data source of DJ, DP, PT and ZJ granites are same to Fig. 6.

Fujian Province at ca. 140 Ma suggests that the igneous event occurred in an extensional setting. This is coincident with the similarities in REE and trace element patterns for the DP unfractionated I-type granite, the Luoyang, PT, and ZJ highly fractionated I-type to A-type granites, and the DJ A-type granite in southwestern Fujian Province (Figs. 6 and 10); it is also in accordance with the observation that almost all these I-type, highly fractionated I-type to A-type, and A-type granites plot within the POG (post-orogenic granites; Maniar and Piccoli, 1989; Fig. 14a) and post-CEG (postcollisional extensional granites; Förster et al., 1997; Fig. 14b) fields. The whole-rock Sr-Nd and zircon Hf isotopes also suggest that the source magma of the Luoyang highly fractionated I-

type to A-type granite is coincident with the DJ A-type granite in the Makeng skarn Fe deposit area (Figs. 7 and 8).

In order to explain the continuous and large-scale anorogenic A-type and I-type granites magmatic events in the South China Block (SCB), Li and Li (2007) proposed a relatively credible “flat subduction-slab break-off and foundering-rollback” model for the subducting paleo-Pacific Plate. The Luoyang highly fractionated I-type to A-type granite (~140 Ma) fits the spatiotemporal distribution of the Jurassic-Cretaceous coastward migration of both extensional and arc-related magmatism and fills in the A-type granite gap in the Early Cretaceous (145–125 Ma; Zhang et al., 2015b).

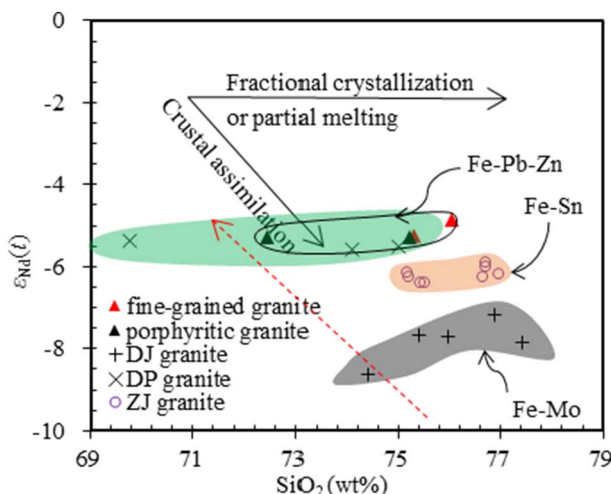


Fig. 13.  $\text{SiO}_2$  versus  $\epsilon_{\text{Nd}}(t)$  diagram for the Luoyang granite. Data source of DJ, DP and ZJ granite are same to Fig. 9.

We suggest that the massive magmatic events during the Late Jurassic and Early Cretaceous, genetically linked with the Fe metallogenesis in southwestern Fujian Province, were generated in an extensional environment and responded to slab rollback and the concomitant retreating arc system of the paleo-Pacific Plate within the SCB.

##### 5.5. Implications for mineralization

The geochemical characteristics show that the DJ granite is characteristic of A-type granites; whereas, the Luoyang granite, along with the PT and ZJ granites, actually corresponds to a transitional-type between highly fractionated I-type to A-type; the DP granite exhibits unfractionated I-type characteristics. The increased  $\epsilon_{\text{Nd}}(t)$  and depleted  $\text{SiO}_2$  values (Fig. 13) suggest that more mafic sources were involved in the transition from the DJ  $\rightarrow$  Luoyang/PT/ZJ  $\rightarrow$  DP granites. Another point supporting this view is the increasing  $\epsilon_{\text{Hf}}(t)$  values (Fig. 8) from the DJ to Luoyang granites. Furthermore, as mentioned above, the diversification of  $\epsilon_{\text{Hf}}(t)$  between the Luoyang granites also suggests that more underplating of mafic magma in the lower tholeiitic crust and/or depleted mantle was also involved in the later extensional environment. In fact, more mafic source involvement will have reduced the oxygen fugacities ( $f\text{O}_2$ ) and  $\text{SiO}_2$  contents of the mineralization related magmas.

Previous works have also proposed that the  $f\text{O}_2$  of different deposits

are slightly different, in the order of:  $\text{Mo} \approx \text{Zn-Pb} > \text{Sn}$  (Meinert et al., 2005; Sun et al., 2015). Molybdenum, Pb, and Zn are all chalcophile elements, with relatively high partition coefficients between sulfide and melts (e.g.,  $D_{\text{Mo}} = 1-2$ ,  $D_{\text{Zn}} = 1-2$  and  $D_{\text{Pb}} = 35-53$ ; Li, 2014). High  $f\text{O}_2$  will restrain the crystallization of sulfide and benefit Mo, Pb, and Zn enrichment in the melts. On the contrary, one siderophile/oxyphile element  $\text{Sn}^{4+}$  will replace  $\text{Fe}^{3+}$  and  $\text{Ti}^{4+}$  in crystallization of magnetite and ilmenite in the high  $f\text{O}_2$  melts (Chen, 2000); therefore, the heterogeneous involvement of a mafic source might cause different oxygen states in melts/fluids and affect the mineral assemblage in the deposit. In addition, fractionation of elements is also controlled by the composition of the melts, which is surely influenced by mafic source involvement in the source magmas.

Therefore, changes in tectonic environment and in the degrees of mafic source involvement caused significant differences in Fe metallogenesis in southwestern Fujian Province: the Makeng Fe deposit related to the DJ granite is associated with molybdenum, whereas the Zhongjia Fe deposit related to the ZJ granite is associated with cassiterite, and the Dapai Fe deposit related to the DP granite is associated with galena and sphalerite, with more mafic sources being involved in the later processes.

## 6. Conclusions

The Luoyang granite yields an LA-ICP-MS zircon U-Pb age of ca. 140 Ma, and exhibits highly fractionated I-type to A-type geochemical characteristics. The variations of major elements and the Rb, Sr, and Ba abundances in the granite were mainly caused by the fractionation of feldspars; whereas, REE variations were mainly caused by the fractionation of allanite, monazite, and apatite. It can be inferred from the whole rock Sr-Nd and zircon Hf isotopes that the source magma of the Luoyang granite was derived from partial melting of Proterozoic metasedimentary Cathaysia basement rocks. It is worth noting that some underplating of mafic magma in the depleted mantle and/or lower tholeiitic crust was also involved. The change in tectonic environment and different degrees of mafic source involvement caused significant differences in Fe metallogenesis in southwestern Fujian Province.

## Acknowledgments

This work was supported by the China Postdoctoral Science Foundation [No. 2015M581144], the National Natural Science Foundation of China (NSFC) [41602070 and 41572315] and the China Geological Survey [DD20160045]. We appreciate the editors and three anonymous reviewers for constructive comments and suggestions.

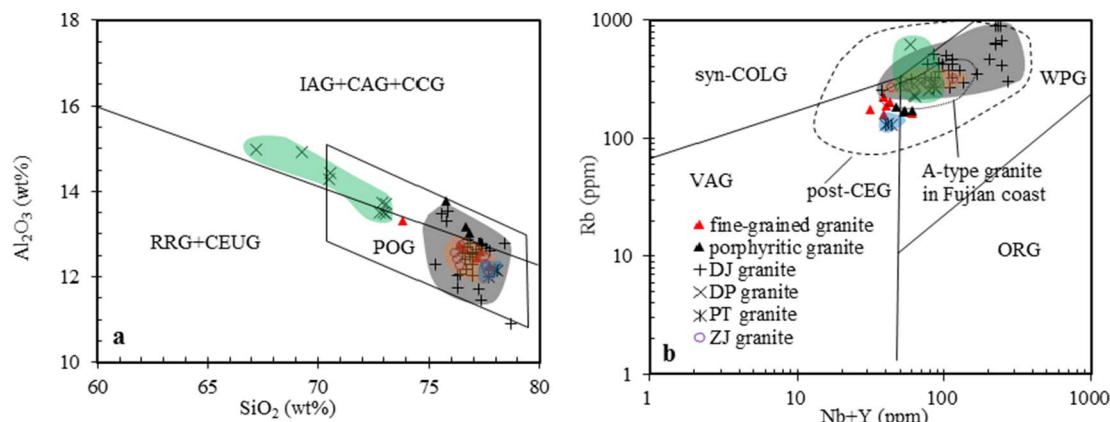


Fig. 14. Tectonic discrimination diagrams of the Luoyang granite. IAG, island-arc granites; CAG, continental arc granites; CCG, continental collision granites; RRG, rift-related granites; CEUG, continental epeirogenic uplift granites; POG, post-orogenic granites; syn-COLG, syn-collisional granites; VAG, volcanic-arc granites; WPG, within-plate granites; ORG, ocean-ridge granites; post-CEG, post-collision extensional granites. Fields in (a) are after Maniar and Piccoli (1989); the post-CEG field is from Förster et al. (1997), field of A-type granite in Fujian coast is after Li et al. (2014), and other fields in (b) are after Pearce et al. (1984). Data source of DJ, DP, PT and ZJ granites are same to Fig. 6.

## References

- Amelin, Y., Lee, D.C., Halliday, A.N., Pidgeon, R.T., 1999. Nature of the Earth's earliest crust from hafnium isotopes in single detrital zircons. *Nature* 399 (6733), 1497–1503.
- Arth, J.G., 1976. Behavior of trace elements during magmatic processes: a summary of theoretical models and their applications. *US Geol. Surv. J. Res.* 4 (1), 41–47.
- Baker, M.B., Hirschmann, M.M., Ghiorso, M.S., Stolper, E.M., 1995. Compositions of near-solidus peridotite melts from experiments and thermodynamic calculations. *Nature* 375 (6529), 308–311.
- Blundy, J.D., Shimizu, N., 1991. Trace element evidence for plagioclase recycling in calc-alkaline magmas. *Earth Planet. Sci. Lett.* 102 (2), 178–197.
- Chappell, B.W., 1999. Aluminium saturation in I-and S-type granites and the characterization of fractionated haplogranites. *Lithos* 46 (3), 535–551.
- Chappell, B.W., White, A.J.R., 1992. I-and S-type granites in the Lachlan Fold Belt. *Geol. Soc. Am. Spec. Pap.* 272, 1–26.
- Chen, J., 2000. The Geochemistry of Tin. Nanjing University Press, Nanjing, pp. 1–341 (in Chinese).
- Chen, J.F., Jahn, B.M., 1998. Crustal evolution of southeastern China: Nd and Sr isotopic evidence. *Tectonophysics* 284 (1–2), 101–133.
- Chen, H.H., Xiao, W.J., 1998. Archipelago orogenesis – examples from Indosian orogenic belts in south China. *Earth Sci. Front.* 5 (S1), 98–105 (in Chinese with English abstract).
- Dall'Agnol, R., de Oliveira, D.C., 2007. Oxidized, magnetite-series, rapakivi-type granites of Carajás, Brazil: implications for classification and petrogenesis of A-type granites. *Lithos* 93 (3–4), 215–233.
- Eby, G.N., 1992. Chemical subdivision of the A-type granitoids - petrogenetic and tectonic implications. *Geology* 20 (7), 641–644.
- Förster, H.J., Tischendorf, G., Trumbull, R.B., 1997. An evaluation of the Rb vs. (Y + Nb) discrimination diagram to infer tectonic setting of silicic igneous rocks. *Lithos* 40 (2), 261–293.
- Frost, C.D., Frost, B.R., Chamberlain, K.R., Edwards, B.R., 1999. Petrogenesis of the 1.43 Ga Sherman batholith, SE Wyoming, USA: a reduced, rapakivi-type anorogenic granite. *J. Petrol.* 40 (12), 1771–1802.
- Frost, B.R., Barnes, C.G., Collins, W.J., Arculus, R.J., Ellis, D.J., Frost, C.D., 2001a. A geochemical classification for granitic rocks. *J. Petrol.* 42 (11), 2033–2048.
- Frost, C.D., Bell, J.M., Frost, B.R., Chamberlain, K.R., 2001b. Crustal growth by magmatic underplating: isotopic evidence from the northern Sherman batholith. *Geology* 29 (6), 515–518.
- Gilder, S.A., Gill, J., Coe, R.S., Zhao, X., Liu, Z., Wang, G., Yuan, K., Liu, W., Kuang, G., Wu, H., 1996. Isotopic and paleomagnetic constraints on the Mesozoic tectonic evolution of south China. *J. Geophys. Res. Solid Earth* 101 (B7), 16137–16154 (1978–2012).
- Green, T.H., Pearson, N.J., 1986. Rare-earth element partitioning between sphene and coexisting silicate liquid at high pressure and temperature. *Chem. Geol.* 55 (1–2), 105–119.
- Green, T.H., Sie, S.H., Ryan, C.G., Cousens, D.R., 1989. Proton microprobe-determined partitioning of Nb, Ta, Zr, Sr and Y between garnet, clinopyroxene and basaltic magma at high pressure and temperature. *Chem. Geol.* 74 (3–4), 201–216.
- Griffin, W.L., Pearson, N.J., Belousova, E., Jackson, S.E., Van Achterberg, E., O'Reilly, S.Y., Shee, S.R., 2000. The Hf isotope composition of cratonic mantle: LAM-MC-ICPMS analysis of zircon megacrysts in kimberlites. *Geochim. Cosmochim. Acta* 64 (1), 133–147.
- Guo, L., Lu, H., Shi, Y., Ma, R., Sun, Y., Shu, L., Jia, D., Zhang, Q., 1996. On the Meso-Neoproterozoic Jiangnan island arc: its kinematics and dynamics. *Geol. J. China Univ.* 2 (1), 1–13 (in Chinese with English Abstract).
- Han, F., Ge, C.H., 1983. Geological and geochemical features of submarine volcanic hydrothermal-sedimentary mineralization of Makeng iron deposit, Fujian province. *Bull. Inst. Miner. Depos. Chin. Acad. Geol. Sci.* 7, 1–118 (in Chinese with English abstract).
- Hanson, G.N., 1978. The application of trace elements to the petrogenesis of igneous rocks of granitic composition. *Earth Planet. Sci. Lett.* 38 (1), 26–43.
- Hart, S.R., 1984. A large-scale isotope anomaly in the Southern Hemisphere mantle. *Nature* 309 (5971), 753–757.
- Hirose, K., 1997. Melting experiments on Iherzolite KLB-1 under hydrous conditions and generation of high-magnesian andesitic melts. *Geology* 25 (1), 42–44.
- Huang, Q.C., 2011. On the geological characteristics and ore-finding perspective of the Luoyang iron ore in Zhangping city, Fujian province. *Geol. Fujian* 30 (2), 113–120 (in Chinese with English abstract).
- Icenhower, J., London, D., 1995. An experimental study of element partitioning among biotite, muscovite, and coexisting peraluminous silicic melt at 200 MPa (H<sub>2</sub>O). *Am. Mineral.* 80 (11–12), 1229–1251.
- Jahn, B.M., Wu, F., Lo, C.H., Tsai, C.H., 1999. Crust–mantle interaction induced by deep subduction of the continental crust: geochemical and Sr–Nd isotopic evidence from post-collisional mafic–ultramafic intrusions of the northern Dabie complex, central China. *Chem. Geol.* 365 (2–3), 119–146.
- King, P.L., White, A.J.R., Chappell, B.W., Allen, C.M., 1997. Characterization and origin of aluminous A-type granites from the Lachlan Fold Belt, southeastern Australia. *J. Petrol.* 38 (3), 371–391.
- King, P.L., Chappell, B.W., Allen, C.M., White, A.J.R., 2001. Are A-type granites the high-temperature felsic granites? Evidence from fractionated granites of the Wangrah Suite. *Aust. J. Earth Sci.* 48 (4), 501–514.
- Lai, S.H., Chen, R.Y., Zhang, D., Di, Y., Gong, Y., Yuan, Y., Chen, L., 2014. Petrogeochemical features and zircon LA-ICP-MS U-Pb ages of granite in the Pantian iron ore deposit, Fujian province and their relationship with mineralization. *Acta Petrol. Sin.* 30 (6), 1780–1792 (in Chinese with English abstract).
- Li, X., 1993. Geochronological framework and isotope system in Southern China: implications for the tectonic evolution of the crust growth. *Bull. Mineral. Petrol. Geochim.* 111–115 (in Chinese with English Abstract), 3.
- Li, Y., 2014. Chalcophile element partitioning between sulfide phases and hydrous mantle melt: applications to mantle melting and the formation of ore deposits. *J. Asian Earth Sci.* 94, 77–93.
- Li, Z.X., Li, X.H., 2007. Formation of the 1300-km-wide intracontinental orogen and post-orogenic magmatic province in Mesozoic South China: a flat-slab subduction model. *Geology* 35 (2), 179–182.
- Li, Z.X., Li, X.H., Zhou, H.W., Kinny, P.D., 2002. Grenvillian continental collision in south China: new SHRIMP U-Pb zircon results and implications for the configuration of Rodinia. *Geology* 30 (2), 163–166.
- Li, X.H., Li, Z.X., Ge, W.C., Zhou, H.W., Li, W.X., Liu, Y., Wingate, M.T.D., 2003a. Neoproterozoic granitoids in South China: crustal melting above a mantle plume at ca. 825 Ma? *Precambrian Res.* 122 (1), 45–83.
- Li, Z.X., Li, X.H., Kinny, P.D., Wang, J., Zhang, S., Zhou, H., 2003b. Geochronology of Neoproterozoic syn-rift magmatism in the Yangtze Craton, South China and correlations with other continents: evidence for a mantle superplume that broke up Rodinia. *Precambrian Res.* 122 (1), 85–109.
- Li, Z., Qiu, J.S., Yang, X.M., 2014. A review of the geochronology and geochemistry of Late Yanshanian (Cretaceous) plutons along the Fujian coastal area of southeastern China: implications for magma evolution related to slab break-off and rollback in the Cretaceous. *Earth-Sci. Rev.* 128, 232–248.
- Lin, D.Y., 2011. Research on late Paleozoic-triassic Tectonic Evolution and Metallogenetic Regularities of Iron-polymetallic Deposits in the Southwestern Fujian Province [PH.D Dissertation]. China University of Geosciences, Beijing.
- Liu, Y.S., Hu, Z.C., Gao, S., Guenther, D., Xu, J., Gao, C.G., Chen, H.H., 2008. In situ analysis of major and trace elements of anhydrous minerals by LA-ICP-MS without applying an internal standard. *Chem. Geol.* 257 (1–2), 34–43.
- Liu, Y.S., Gao, S., Hu, Z.C., Gao, C.G., Zong, K.Q., Wang, D.B., 2010. Continental and oceanic crust recycling-induced melt-peridotite interactions in the Trans-North China Orogen: U-Pb dating, Hf isotopes and trace elements in zircons from mantle xenoliths. *J. Petrol.* 51, 537–571.
- Ludwig, K.R., 2003. Isoplot 3.00: A Geochronological Toolkit for Microsoft Excel.
- Mahood, G., Hildreth, W., 1983. Large partition coefficients for trace elements in high-silica rhyolites. *Geochim. Cosmochim. Acta* 47 (1), 11–30.
- Maniar, P.D., Piccoli, P.M., 1989. Tectonic discrimination of granitoids. *Geol. Soc. Am. Bull.* 101 (5), 635–643.
- Mao, J., Tao, X., Xie, F., Xu, N., Chen, S., 2001. Rock-forming and ore-forming processes and tectonic environments in southwest Fujian. *Acta Petrol. Mineral.* 20 (3), 329–336 (in Chinese with English Abstract).
- Mao, J., Xie, G., Li, X., Zhang, C., Mei, Y., 2004. Mesozoic large scale mineralization and multiple lithospheric extension in South China. *Earth Sci. Front.* 11 (1), 45–55 (in Chinese with English Abstract).
- Mao, J., Chen, R., Li, J., Ye, H., Zhao, X., 2006. Geochronology and geochemical characteristics of late Mesozoic granitic rocks from southwestern Fujian and their tectonic evolution. *Acta Petrol. Sin.* 22 (6), 1723–1734 (in Chinese with English abstract).
- Mao, J., Xie, G., Guo, C., Chen, Y., 2007. Large-scale tungsten-tin mineralization in the Nanling region South China: metallogenetic ages and corresponding geodynamic process. *Acta Petrol. Sin.* 23 (10), 2329–2338 (in Chinese with English Abstract).
- Mao, J.W., Xie, G.Q., Guo, C.L., Yuan, S.D., Cheng, Y.B., Chen, Y.C., 2008. Spatial-temporal distribution of Mesozoic ore deposits in South China and their metallogenetic settings. *Geol. J. China Univ.* 14 (4), 510–526 (in Chinese with English Abstract).
- Meinert, L., Dipple, G., Nicolescu, S., 2005. World skarn deposits. In: *Econ. Geol.* 100th Anniv. Vol. pp. 299–336.
- Pearce, J.A., Harris, N.B.W., Tindle, A.G., 1984. Trace element discrimination diagrams for the tectonic interpretation of granitic rocks. *J. Petrol.* 25 (4), 956–983.
- Peccerillo, A., Taylor, S.R., 1976. Geochemistry of eocene calc-alkaline volcanic rocks from the Kastamonu area, northern Turkey. *Contrib. Mineral. Petro.* 58 (1), 63–81.
- Pitcher, W.S., 1982. Granite type and tectonic environment. In: Hsu, K.J. (Ed.), *Mountain Building Processes*. Academic Press, London, pp. 19–40.
- Plank, T., Langmuir, C.H., 1998. The chemical composition of subducting sediment and its consequences for the crust and mantle. *Chem. Geol.* 145 (3–4), 325–394.
- Shen, W.Z., Ling, H.F., Li, W.X., Wang, D.Z., 2000. Crust evolution in Southeast China: evidence from Nd model ages of granitoids. *Sci. China Ser. D* 43 (1), 36–49.
- Shu, L.S., 2006. Predevonian tectonic evolution of South China: from Cathaysian Block to Caledonian period folded orogenic belt. *Geol. J. China Univ.* 12 (4), 418–431 (in Chinese with English Abstract).
- Shu, L.S., Zhou, G., 1988. The first discovery of the high-pressure minerals in the collage zone of Proterozoic terrains in north Jiangxi and its tectonic significance. *J. Nanjing Univ. (Nat. Sci. Ed.)* 24 (3), 421–429 (in Chinese with English Abstract).
- Shu, L.S., Zhou, X.M., 2002. Late Mesozoic tectonism of southeast China. *Geol. Rev.* 48 (3), 249–260 (in Chinese with English Abstract).
- Shu, L., Zhou, X., Deng, P., Yu, X., Wang, B., Zu, F., 2004. Geological features and tectonic evolution of Meso-Cenozoic basins in southeastern China. *Geol. Bul. China* 23, 876–884 (in Chinese with English Abstract).
- Shu, L.S., Faure, M., Wang, B., Zhou, X.M., Song, B., 2008. Late Palaeozoic-Early Mesozoic geological features of South China: response to the Indosian collision events in Southeast Asia. *Compt. Rendus Geosci.* 340 (2), 151–165.
- Shu, L.S., Wang, Y., Sha, J.G., Jiang, S.Y., Yu, J.H., Wang, Y.B., 2009a. Jurassic sedimentary features and tectonic settings of southeastern China. *Sci. China Ser. D* 52 (12), 1969–1978.
- Shu, L.S., Zhou, X.M., Deng, P., Wang, B., Jiang, S.Y., Yu, J.H., Zhao, X.X., 2009b. Mesozoic tectonic evolution of the Southeast China Block: new insights from basin analysis. *J. Asian Earth Sci.* 34 (3), 376–391.

- Shu, L.S., Faure, M., Yu, J.H., Jahn, B.M., 2011. Geochronological and geochemical features of the Cathaysia block (South China): new evidence for the Neoproterozoic breakup of Rodinia. *Precambrian Res.* 187 (3), 263–276.
- Shui, T., Yan, J., Shi, H., Pan, M., Wang, J., 1993. The elementary features and evolution models of Zhenghe-Dapu fault zone. *Volcanol. Miner. Resour.* 14 (2), 53–62 (in Chinese with English Abstract).
- Sun, S.-s., McDonough, W.F., 1989. Chemical and isotopic systematics of oceanic basalts: implications for mantle composition and processes. *Geol. Soc. Lond. Spec. Publ.* 42, 313–345.
- Sun, W.D., Huang, R.F., Li, H., Hu, Y.B., Zhang, C.C., Sun, S.J., Zhang, L.P., Ding, X., Li, C.Y., Zartman, R.E., 2015. Porphyry deposits and oxidized magmas. *Ore Geol. Rev.* 65, 97–131.
- Sylvester, P.J., 1989. Post-collisional alkaline granites. *J. Geol.* 97 (3), 261–280.
- Wang, Q., Zhao, Z.H., Jian, P., Xiong, X.L., Bao, Z.W., Dai, T.M., Xu, J.F., Ma, J.L., 2005. Geochronology of Cretaceous, A-type granitoids or alkaline intrusive rocks in the hinterland, South China: constraints for late-Mesozoic tectonic evolution. *Acta Petrol. Sin.* 21 (3), 795–808 (in Chinese with English abstract).
- Wang, Q., Wyman, D.A., Li, Z.X., Bao, Z.W., Zhao, Z.H., Wang, Y.X., Jian, P., Yang, Y.H., Chen, L.L., 2010. Petrology, geochronology and geochemistry of ca. 780 Ma A-type granites in South China: petrogenesis and implications for crustal growth during the breakup of the supercontinent Rodinia. *Precambrian Res.* 178 (1–4), 185–208.
- Wang, S., Zhang, D., Absai, V., Yan, P.C., Ma, S., Feng, H.B., Yu, T.D., Bai, Y., Di, Y.J., 2015a. Zircon U-Pb geochronology, geochemistry and Hf isotope compositions of the Dayang and Juzhou granites in Longyan, Fujian and their geological implications. *Geochimica* 44 (5), 450–468 (in Chinese with English abstract).
- Wang, Z., Zuo, R., Zhang, Z., 2015b. Spatial analysis of Fe deposits in Fujian province, China: implications for mineral exploration. *J. China Univ. Geosci.* 26 (6), 813–820.
- Whalen, J.B., Currie, K.L., Chappell, B.W., 1987. A-type granites - geochemical characteristics, discrimination and petrogenesis. *Contrib. Mineral. Petrol.* 95 (4), 407–419.
- White, A.J.R., Chappell, B.W., 1983. Granitoid types and their distribution in the Lachlan Fold Belt, southeastern Australia. *Geol. Soc. Am. Mem.* 159, 21–34.
- Wong, J., Sun, M., Xing, G.F., Li, X.H., Zhao, G.C., Wong, K., Yuan, C., Xia, X.P., Li, L.M., Wu, F.Y., 2009. Geochemical and zircon U-Pb and Hf isotopic study of the Baijihuajian metaluminous A-type granite: extension at 125–100 Ma and its tectonic significance for South China. *Lithos* 112 (3–4), 289–305.
- Workman, R.K., Hart, S.R., 2005. Major and trace element composition of the depleted MORB mantle (DMM). *Earth Planet. Sci. Lett.* 231 (1–2), 53–72.
- Wu, F.Y., Jahn, B.M., Wilde, S.A., Lo, C.H., Yui, T.F., Lin, Q., Ge, W.C., Sun, D.Y., 2003. Highly fractionated I-type granites in NE China (I): geochronology and petrogenesis. *Lithos* 66 (3), 241–273.
- Xie, X., Xu, X., Zou, H., Xing, G., 2001. Trace element and Nd-Sr-Pb isotope studies of Mesozoic and Cenozoic basalts in coastal area of SE China. *Acta Petrol. Sin.* 17 (4), 617–628 (in Chinese with English Abstract).
- Xu, J., Sun, S., Li, J., 1987. It is the southern China orogenic belt and is not the southern China platform. *Sci. China Ser. D* 10, 1107–1115 (in Chinese).
- Xu, X.S., O'Reilly, S.Y., Griffin, W.L., Wang, X.L., Pearson, N.J., He, Z.Y., 2007. The crust of Cathaysia: age, assembly and reworking of two terranes. *Precambrian Res.* 158 (1), 51–78.
- Yang, Z.L., Zhang, D.Q., Feng, C.Y., She, H., Li, J., 2008. SHRIMP zircon U-Pb dating of quartz porphyry from Zhongjia Tin-polymetallic deposit in Longyan area, Fujian province, and its geological significance. *Mineral Deposits* 27 (3), 329–335 (in Chinese with English abstract).
- Yuan, Y., 2014. The Metallogenetic Chronology of Dapai Iron Polymetallic Ore Deposits in Yongding County, Fujian Province and its Genetic Significance. China University of Geosciences, Beijing.
- Yuan, Y., Feng, H.B., Zhang, D., Di, Y., Wang, C., Ni, J., 2013. Geochronology of Dapai iron-polymetallic deposit in Yongding city, Fujian province and its geological significance. *Acta Mineral. Sin.* 33 (Suppl. 2), 73–75 (in Chinese).
- Yurimoto, H., Duke, E.F., Papike, J.J., Shearer, C.K., 1990. Are discontinuous chondrite-normalized REE patterns in pegmatitic granite systems the results of monazite fractionation? *Geochim. Cosmochim. Acta* 54 (7), 2141–2145.
- Zartman, R.E., Doe, B.R., 1981. Plumbotectonics - the model. *Tectonophysics* 75 (1), 135–162.
- Zhang, Z.J., Zuo, R.G., 2014. Sr-Nd-Pb isotope systematics of magnetite: implications for the genesis of Makeng Fe deposit, southern China. *Ore Geol. Rev.* 57, 53–60.
- Zhang, Y., Xu, X., Jia, D., Shu, L., 2009. Deformation record of the change from Indosian collision-related tectonic system to Yanshanian subduction-related tectonic system in South China during the Early Mesozoic. *Earth Sci. Front.* 16 (1), 234–247 (in Chinese with English Abstract).
- Zhang, C.S., Li, L., Zhang, C.Q., Wang, J.R., 2012a. LA-ICP-MS zircon U-Pb ages and Hf isotopic compositions of Dayang granite from Longyan, Fujian Province. *Geoscience* 3 (26), 433–444 (in Chinese with English abstract).
- Zhang, C.S., Mao, J.W., Xie, G.Q., Zhao, C., Yu, M., Wang, J., Liu, W., 2012b. Geology and molybdenite Re-Os ages of Makeng skarn-type Fe-Mo deposit in Fujian province. *J. Jilin Univ. (Earth Sci. Ed.)* 42, 224–236 (in Chinese with English abstract).
- Zhang, C.S., Su, H.M., Yu, M., Hu, Z., 2012c. Zircon U-Pb age and Nd-Sr-Pb isotopic characteristics of Dayang-Juzhou granite in Longyan, Fujian province and its geological significance. *Acta Petrol. Sin.* 28 (1), 225–242 (in Chinese with English abstract).
- Zhang, D., Wu, G.G., Di, Y.J., Wang, C.M., Yao, J., Zhang, Y., Lv, L., Yuan, Y., Shi, J., 2012d. Geochronology of diagenesis and mineralization of the Luoyang iron deposit in Zhangping city, Fujian province and its geological significance. *Earth Sci. J. China Univ. Geosci.* 37 (6), 1217–1231 (in Chinese with English abstract).
- Zhang, Z., Zuo, R., Cheng, Q., 2015a. Geological features and formation processes of the Makeng Fe deposit. *China. Resour. Geol.* 65 (3), 266–284.
- Zhang, Z.J., Zuo, R.G., Cheng, Q.M., 2015b. The mineralization age of the Makeng Fe deposit, South China: implications from U-Pb and Sm-Nd geochronology. *Int. J. Earth Sci. (Geol. Rundsch.)* 104, 663–682.
- Zhao, Z.F., Zheng, Y.F., 2009. Remelting of subducted continental lithosphere: Petrogenesis of Mesozoic magmatic rocks in the Dabie-Sulu orogenic belt. *Sci. China Ser. D* 52 (9), 1295–1318.
- Zhao, X.L., Yu, S.Y., Yu, M.G., Jiang, Y., Liu, K., Mao, J.R., 2016. Geological characteristics and metallogenic epochs of the Dapai Fe-Pb-Zn polymetallic deposit in Yongding County, Fujian Province. *Geol. China* 43 (1), 174–187 (in Chinese with English abstract).
- Zhou, X.M., Li, W.X., 2000. Origin of Late Mesozoic igneous rocks in Southeastern China: implications for lithosphere subduction and underplating of mafic magmas. *Tectonophysics* 326 (3–4), 269–287.
- Zhu, B.Q., 1998. Theory and Application of Isotopic Systematic in Earth Science. Science Press, Beijing, pp. 330 (in Chinese).
- Zindler, A., Hart, S., 1986. Chemical geodynamics. *Annu. Rev. Earth Planet. Sci.* 14 (1), 493–571.
- Zuo, R., 2016. A nonlinear controlling function of geological features on magmatic-hydrothermal mineralization. *Sci. Rep. UK* 6, 27127.
- Zuo, R.G., Zhang, Z.J., Zhang, D.J., Carranza, E.J.M., Wang, H.C., 2015. Evaluation of uncertainty in mineral prospectivity mapping due to missing evidence: a case study with skarn-type Fe deposits in Southwestern Fujian Province, China. *Ore Geol. Rev.* 71, 502–515.